Annexe A

Performances de AVBP multiclasse

L'implémentation du module multi-fluide dans AVBP a nécessité un profond remaniement du code pour permettre de prendre en compte plusieurs sections ou classes de la phase liquide. Le calcul associé soulève donc la question de la performance des calculs multi-classes par rapport aux calculs monodisperses. Le temps d'un calcul multi-fluide est très proche d'un calcul multi-classe, étant donné que la seule différence est une routine supplémentaire pour l'évaporation. On parlera donc ici de classes pour le liquide. On se propose d'évaluer cette performance sur le cas test de la THI présenté dans le chapitre 4. Les calculs sont effectués sur le cluster de l'IFP. Il est composé de 114 noeuds de calcul possédant chacun 4 processeurs quadri-coeurs AMD opteron barcelona 8356 cadencés à 2.3ghz. Ces processeurs possèdent 4x512ko de cache L2, et 2Mo de cache L3.

On analyse ici les effets de deux paramètres : le nombre de classes et le ncgroup, qui est un paramètre fixé par l'utilisateur dans AVBP, et permet de grouper des séries de calculs sur les cellules avant de les envoyer aux processeurs : plutôt que d'envoyer les cellules une par une, ou toutes d'un coup, on choisit de les envoyer par petits paquets, pour optimiser l'utilisation de la mémoire cache du processeur. L'importance du choix de ce paramètre est connue, et ses effets dépendent du cas utilisé, du nombre de modèles activés (qui fait varier la quantité de calculs par cellule), et surtout du processeur utilisé. Ils ne dépendent cependant pas du nombre de processeurs utilisés. On ne s'intéresse pas ici à la performance parallèle du code, considérant que le rapport entre les communications et les calculs de chaque processeur ne change pas avec le nombre de sections.

On définit l'efficacité réduite :

$$E = T.\frac{N_{proc}}{N_{cell} * N_{ite}} \tag{A.1}$$

où T est le temps de calcul. L'efficacité réduite est tracée sur la Fig. A.1 en fonction du nombre de classes, pour trois ncgroup différents. On remarque qu'à ncgroup=5, l'augmentation de l'efficacité réduite est proportionnelle au nombre de classes dans le calcul. Cela confirme un bon comportement du code en fonction du nombre de classes. Cependant, pour des ncgroup supérieurs (ici 40 et 90), l'augmentation n'est plus linéaire. La figure A.2 confirme ce comportement, où l'efficacité réduite en fonction du

ncgroup, pour 0, 1, 5, et 10 classes est tracée. On remarque qu'à 0 et 1 classes, le temps de calcul varie peu avec le ncgroup, alors qu'à 5 et 10 classes, le temps de calcul varie fortement, rendant nécessaire une optimisation du paramètre. En pratique, il semble que le nombre d'équation à résoudre par cellule est tellement important que la stratégie de groupage des cellules ne soit pas optimale, et qu'une approche séquentielle est préférable.

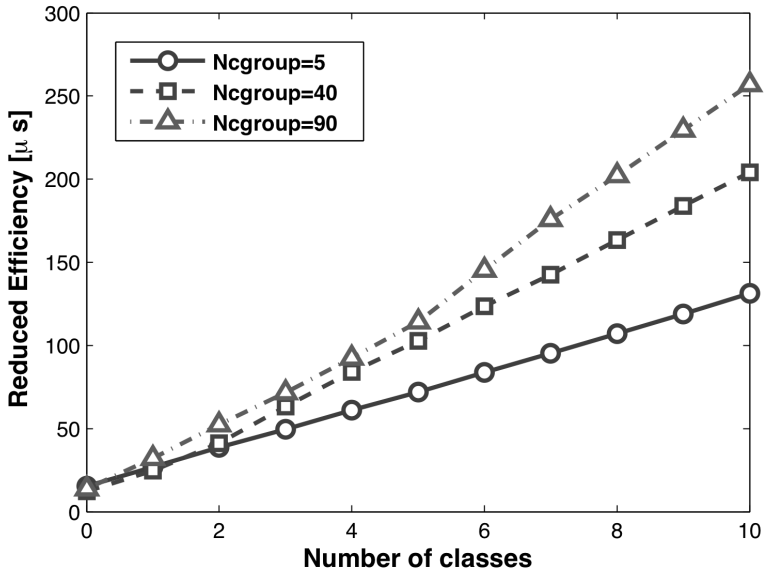

FIGURE A.1 – Efficacité réduite en fonction du nombre de classes pour un ncgroup de 5 (cercles), 40 (carrés) et 90 (triangles), obtenue sur 16 processeurs AMD Opteron Barcelona 8356 à 2.3 ghz.

Pour évaluer l'influence des processeurs sur l'optimisation du cache, on effectue le même test sur 4 processeurs Intel Xeon W3520 cadencés à 2.66ghz, et ayant 4x256ko de cache L2 et 8Mo de cache L3. Ces processeurs sont intrinsèquement plus puissants que les processeurs utilisés précédemment. La figure A.3 montre l'efficacité réduite en fonction du nombre de classes pour différents ncgroup. La puissance supérieure de ces processeurs conduit à un facteur 2 sur l'efficacité réduite. L'augmentation de l'efficacité réduite reste ici relativement linéaire pour tous les ncgroup, même si le coût par classe augmente avec le ncgroup.

D'après la figure A.4, on remarque que l'effet du ncgroup sur l'efficacité réduite est en effet beaucoup moins important qu'avec les opteron, et ce quel que soit le nombre de classe. L'augmentation de l'efficacité entre ncgroup=5 et ncgroup=90 pour un calcul à 10 classes est seulement de 30%, alors qu'elle était de 92% avec les opteron. Cet effet du ncgroup est donc bien caractéristique de la machine, et ne pose pas de gros problème d'optimisation sur des processeurs de dernière génération. Le ncgroup reste cependant un paramètre à contrôler et optimiser systématiquement, quelle que soit la machine ou le type de calcul.

On s'intéresse enfin à la mémoire vive utilisée par le calcul, avec le même cas test de la THI. La figure A.5 montre la place occupée en mémoire vive par AVBP en fonction du nombre de classe. On remarque

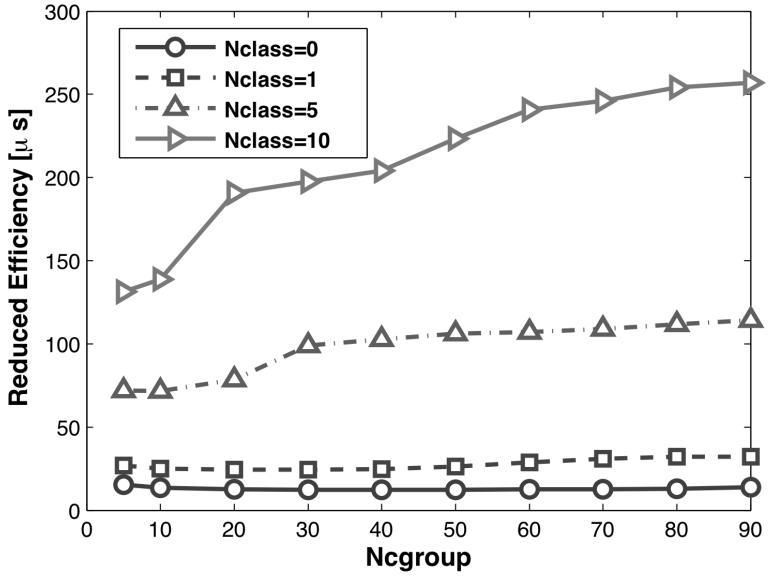

FIGURE A.2 – Efficacité réduite en fonction du ncgroup pour 0 (cercles), 1 (carrés), 5 (triangles vers le haut) et 10 classes (triangles vers la droite), obtenue sur 16 processeurs AMD Opteron Barcelona 8356 à 2.3 ghz.

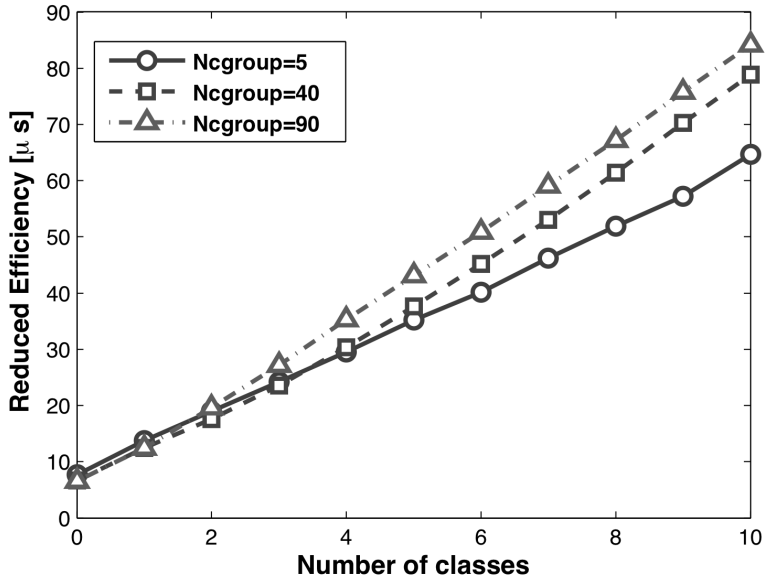

FIGURE A.3 – Efficacité réduite en fonction du nombre de classes pour un ncgroup de 5 (cercles), 40 (carrés) et 90 (triangles), obtenue sur 4 processeurs Intel Xeon W3520 cadencés à 2.66ghz.

que l'évolution est bien linéaire, confirmant une bonne implémentation de l'architecture multiclasse.

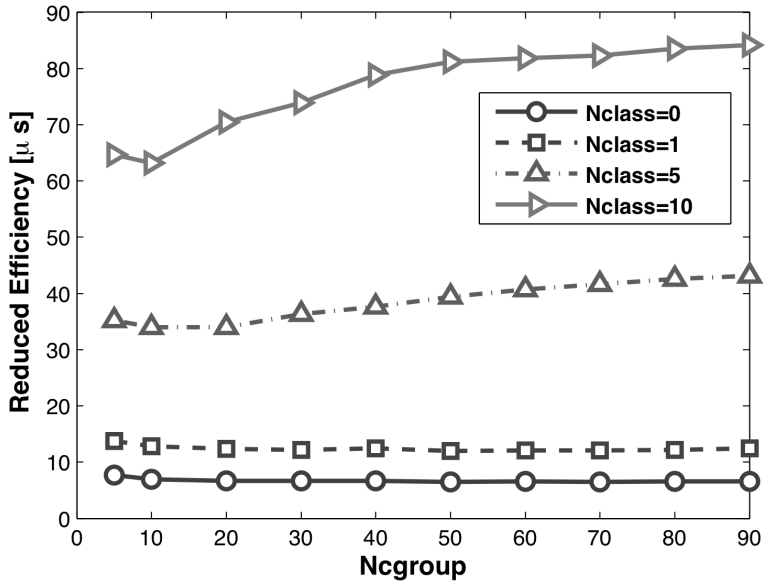

FIGURE A.4 – Efficacité réduite en fonction du ncgroup pour 0 (cercles), 1 (carrés), 5 (triangles vers le haut) et 10 classes (triangles vers la droite), obtenue sur 4 processeurs Intel Xeon W3520 cadencés à 2.66ghz.

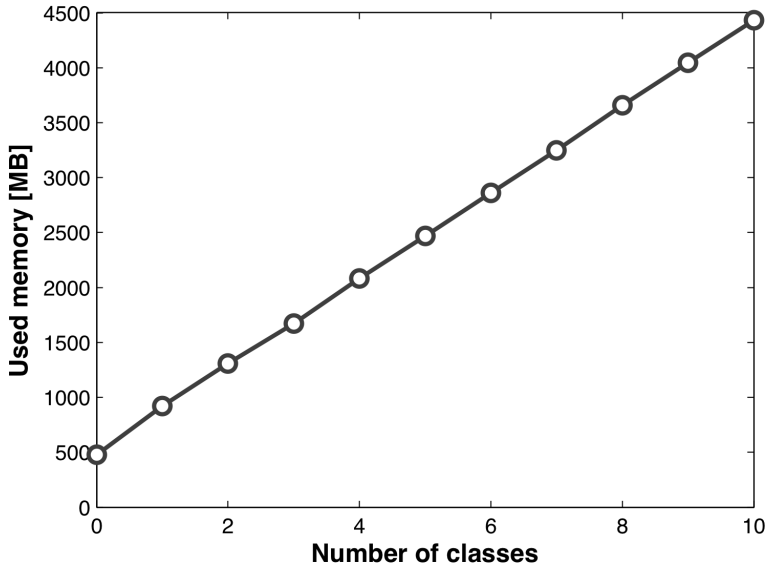

FIGURE A.5 – Mémoire vive utilisée par AVBP en fonction du nombre de classes.

Annexe B

Modèles de trainée et d'évaporation

B.1 Forces extérieures

La trajectographie des particules est la conséquence de nombreuses forces, dues à l'interaction entre le fluide porteur et les particules immergées. Ces forces sont résumées dans Maxey and Riley [1983]. Pour les écoulements qui nous intéressent, où le rapport entre la masse volumique des gouttes et du fluide porteur est très grand, Hinze [2005] et Desjonqueres et al. [1986] ont montré que les uniques forces à prendre en compte sont la trainée et la gravité. Nous négligerons ici la gravité, et nous ne modéliserons que les efforts de trainée.

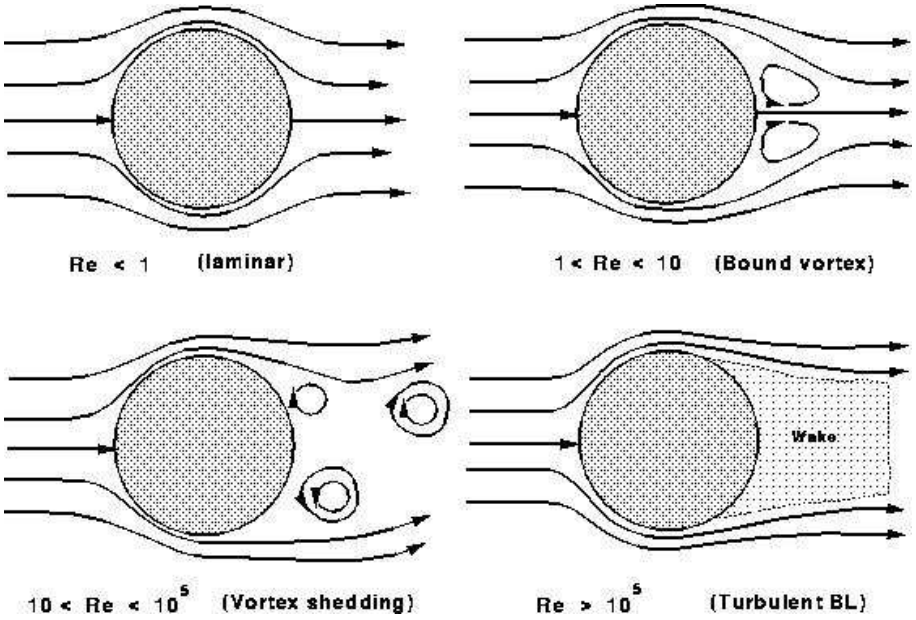

FIGURE B.1 – Ecoulement autour d'une sphère en fonction du nombre de Stokes.

La force de traînée s'exprime dans sa forme générale par :

$$F_{D,i} = \frac{1}{2} C_D \rho_g S_i |V_r| (U_{g,i} - c_{p,i}) \tag{B.1}$$

où $|V_r| = \sqrt{(U_{g,i} - c_{p,i})^2}$ est la norme de la vitesse relative entre le gaz et la goutte, S_i est la surface de la goutte projetée sur le plan perpendiculaire à l'axe i, appelée aussi surface efficace, et $U_{g,i}$ est la vitesse du gaz.

Pour des gouttes sphériques de diamètre d et de masse m_p, la force de traînée s'écrit :

$$F_{D,i} = \frac{1}{2} C_D \rho_g \frac{\pi d^2}{4} |V_r| (U_{g,i} - c_{p,i}) \tag{B.2}$$

d'où

$$\frac{F_{D,i}}{m_p} = \frac{6 F_{D,i}}{\rho_l \pi d^3} = \frac{3}{4} \frac{\rho_g}{\rho_l} C_D |V_r| \frac{(U_{g,i} - c_{p,i})}{d} \tag{B.3}$$

Le temps de relaxation de la particule, ou temps caractéristique de Stokes τ_p est défini par la formule :

$$\tau_p = \frac{4}{3} \frac{\rho_l}{\rho_g} \frac{d}{C_D |V_r|} \tag{B.4}$$

Le type d'écoulement autour de la goutte évolue en fonction du nombre de Reynolds (fig. B.1). Pour prendre en compte cet effet, le coefficient de traînée C_D pour une goutte isolée est donné par la corrélation empirique de Schiller and Nauman [1935] dans le cas turbulent :

$$C_D = \frac{24}{Re_d} \left(1 + 0.15 Re_d^{0.687}\right) \tag{B.5}$$

avec Re_d le nombre de Reynolds particulaire :

$$Re_d = \frac{\rho_g d |V_r|}{\mu_g} \tag{B.6}$$

où μ_g est la viscosité dynamique du gaz. Cette corrélation a été validée comparativement aux résultats expérimentaux de Roos and Wilmarth [1971]. Le temps de relaxation devient donc :

$$\tau_p = \frac{\rho_l d^2}{18 \mu_g} \left(1 + 0.15 {Re_d}^{0.687}\right)^{-1} \tag{B.7}$$

.

et on peut écrire :

$$F_{D,i} = \frac{m_p}{\tau_p} (U_{g,i} - c_{p,i}) \tag{B.8}$$

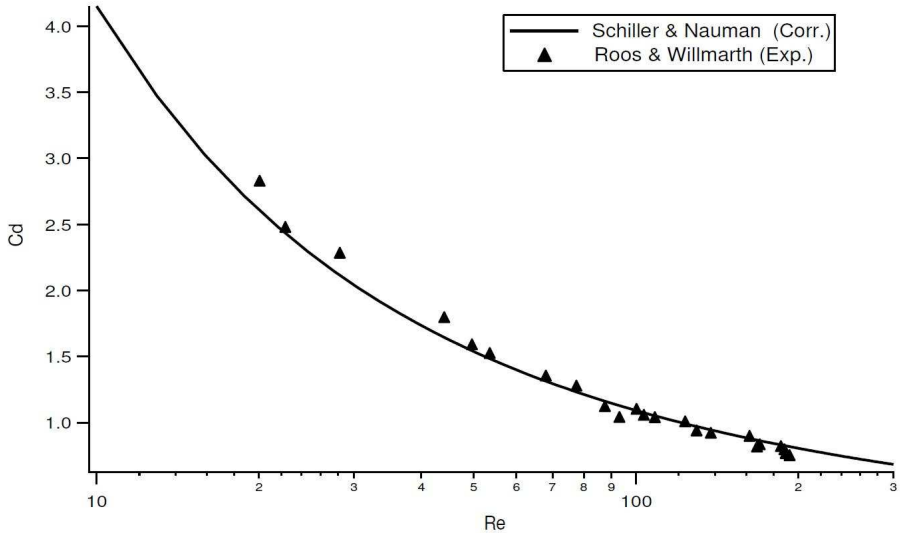

FIGURE B.2 – Corrélation empirique du coefficient de trainée de Schiller and Nauman [1935], en comparaison aux résultats expérimentaux de Roos and Wilmarth [1971].

Le temps de relaxation τ_p est un paramètre capital concernant le comportement de la phase dispersée dans un écoulement turbulent. Dans un tel écoulement, on peut caractériser le comportement des particules par le nombre de Stokes, qui est le rapport entre le temps de relaxation des particules et une échelle de temps du champ turbulent :

$$St_K = \frac{\tau_p}{\tau_K} \tag{B.9}$$

$$St_L = \frac{\tau_p}{\tau_l} \tag{B.10}$$

$$St_\varepsilon = \frac{\tau_p}{\tau_\varepsilon} \tag{B.11}$$

St_K est le nombre de Stokes relatif au temps de Kolmogorov, St_L est le nombre de Stokes relatif au temps Lagrangien et St_ε est le nombre de Stokes relatif au temps de l'échelle de coupure. Si le nombre de Stokes est «1, la particule pourra être capturée par l'échelle du gaz considérée, si le Stokes est »1, la particule ne sera pas influencé par le gaz. Pour les Stokes intermédiaires, la particule sera seulement dévié par le gaz. Ces échelles ont une grande importance quand on s'interesse au two-way coupling entre le liquide et le gaz. En effet, d'après Fig. B.3 (Elgobashi and Truesdell [1993]), pour une certaine fraction volumique de liquide, on doit prendre en compte l'effet du gaz sur le liquide, mais aussi celui du liquide sur le gaz. Des considérations sur la modélisation seront abordées dans le chapitre 2.4.

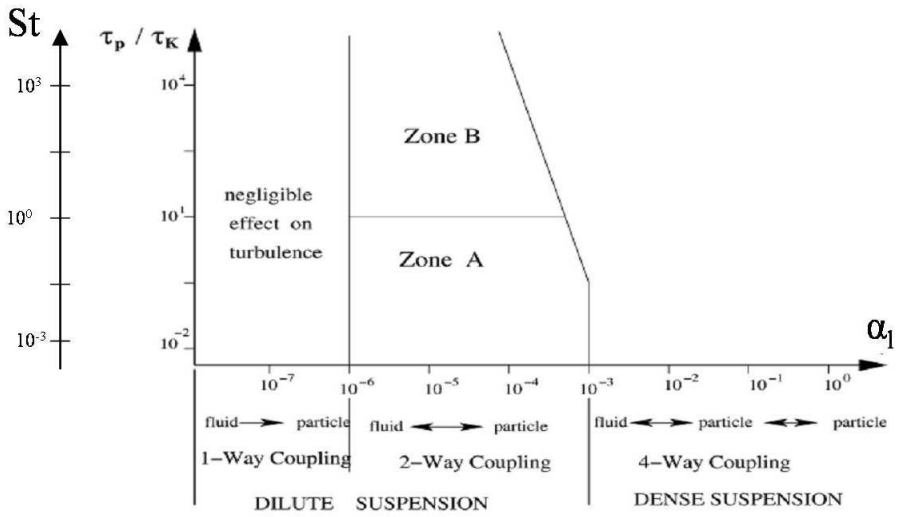

FIGURE B.3 – Niveau de couplage entre la phase dispersée et la phase gazeuse en fonction de la fraction volumique de liquide selon Elgobashi and Truesdell [1993].

B.2 Évaporation

L'évaporation des gouttes est capitale dans les applications énergétiques, et de nombreux modèles existent, avec chacun leur degré de précision. Une revue des modèles existants est disponible dans Sazhin [2006]. On détaille le modèle utilisé ici. Le modèle d'évaporation utilisé est un modèle hydrodynamique, écrit sous l'hypothèse de goutte isolée dans un milieu gazeux sans combustion et de température de la goutte uniforme Spalding [1953], Abramzon and Sirignano [1989] (hypothèse d'une conductivité thermique infinie). L'interface liquide/gaz est supposée en état d'équilibre thermodynamique, ce qui permet d'utiliser la relation de Clausius-Clapeyron :

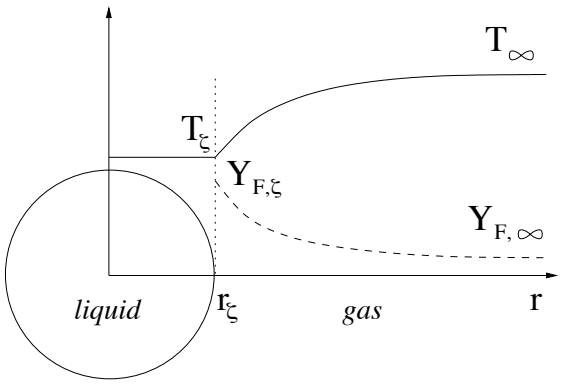

FIGURE B.4 – Goutte isolée à la température T_ζ s'évaporant dans un écoulement de gaz à la température T_∞ et avec une fraction massique de carburant $Y_{F,\infty}$.

La température de la goutte est calculée par l'équation de l'enthalpie de la phase liquide qui prend bien en compte les phases de réchauffement et d'évaporation.

Transfert massique

Le taux de transfert de masse $\dot{m}_p$ dépend seulement des variables à $r = r_\zeta$ et $r \to \infty$ Kuo [2005] :

$$\dot{m}_p = -\pi d\, Sh\, [\rho D_F] \ln(1 + B_M) \tag{B.12}$$

Sh est le nombre de Sherwood donné par :

$$Sh = 2 + K Re_p^{1/2} {Sc_F}^{1/3} \tag{B.13}$$

où le terme $K Re_p^{1/2} {Sc_F}^{1/3}$ prend en compte les effets convectifs liés à la vitesse relative entre les phases. Dans la littérature, K varie entre 0.552 et 0.6 Ranz and Marshall [1952]. Dans AVBP la valeur $K = 0.55$ a été retenue.
Le produit $[\rho D_F]$ est obtenu à partir du nombre de Schmidt du carburant Sc_F :

$$[\rho D_F] = \frac{\mu}{Sc_F} \tag{B.14}$$

B_M est le nombre de Spalding de masse lié à la différence de fraction massique de carburant (indice F) entre l'interface et l'infini :

$$cpEB_M = \frac{Y_{F,\zeta} - Y_{F,\infty}}{1 - Y_{F,\zeta}} \tag{B.15}$$

où $Y_{F,\zeta}$ peut être écrit en fonction de la fraction molaire $X_{F,\zeta}$:

$$Y_{F,\zeta} = \frac{X_{F,\zeta} W_F}{X_{F,\zeta} W_F + (1 - X_{F,\zeta})\, \overline{W}_{nF,\zeta}} \tag{B.16}$$

où $\overline{W}_{nF,\zeta}$ est la masse molaire moyenne du *pseudo*-mélange constitué de toutes les espèces sauf le carburant. En faisant l'hypothèse que la composition de ce mélange n'évolue pas entre ζ et ∞, on obtient :

$$\overline{W}_{nF,\zeta} = \overline{W}_{nF,\infty} = \frac{1 - Y_{F,\infty}}{1 - Y_{F,\infty} \frac{W}{W_F}} W \tag{B.17}$$

où $X_{F,\zeta}$ est donnée par la loi de Raoult pour un mélange idéal de gaz parfaits :

$$X_{F,\zeta} = \frac{P_{F,\zeta}}{P} \tag{B.18}$$

où $P_{F,\zeta}$ est la pression partielle de carburant gazeux à l'interface donnée par la relation de Clausius-Clapeyron :

$$P_{F,\zeta} = P_{cc}\, exp\left(\frac{W_F L_v}{\mathcal{R}} \left(\frac{1}{T_{cc}} - \frac{1}{T_\zeta}\right)\right) \tag{B.19}$$

P_{cc} et T_{cc} sont respectivement la pression et la température de référence correspondant à un point sur la courbe de saturation du carburant. L_v est la chaleur latente massique d'évaporation représentant la différence d'enthalpie entre les phases à la température de référence T_{ref} :

$$L_v = \Delta h_{s,F}\left(T_{ref}\right) = h_{s,F}\left(T_{ref}\right) - h_{s,p}\left(T_{ref}\right) \tag{B.20}$$

Dans Eq. B.19, la température de l'interface T_ζ a été supposée égale à la température de la goutte : $T_\zeta = T_p$. Dans Eq. B.15 et B.17, la condition à l'infini correspond à l'état thermodynamique du gaz non perturbé par la goutte. Pour des écoulements dilués, la distance entre les gouttes est suffisament grande pour garantir que les gouttes n'interagissent pas entre elles. En conséquence l'état infini (∞) correspond aux valeurs moyennes locales Eulériennes du gaz dans la cellule.

Échange de chaleur

Le flux conductif de gaz à l'interface est approché par l'expression obtenue pour une particule sans changement de phase :

$$\phi_g^c = -\phi_l^c = \pi d Nu \lambda \left(T_\zeta - T_\infty\right) \frac{ln(1+B_T)}{B_T} \tag{B.21}$$

où

$$B_T = \frac{\overline{C_p}\left(T_\zeta - T_\infty\right)}{\Delta h_{s,F}\left(T_\zeta\right) + \phi_l^c/\dot{m}_p} \tag{B.22}$$

est le nombre de Spalding de température et est évalué par $B_T = max\{\varepsilon, (1+B_M)^{Sh/(NuLe_F)} - 1\}$, où ε est un petit nombre utilisé pour éviter les erreurs numériques quand B_T tend vers 0 dans Eq. B.21. ϕ_l^c est le flux conductif entrant dans la goutte. Nu est le nombre de Nusselt exprimé de manière similaire au nombre de Sherwood (Eq. B.13) :

$$Nu = 2 + 0.55 Re_p^{1/2} Pr^{1/3} \tag{B.23}$$

La conductivité thermique du gaz λ est obtenue à partir du nombre de Prandtl Pr :

$$\lambda = \frac{\mu \overline{C_p}}{Pr} \tag{B.24}$$

Coefficient de transport : la règle des 2/3

Dans Eq. B.12 et B.21, les propriétes de transport $[\rho D_F]$ et λ sont supposées constantes dans l'intégration des équations de conservation. En réalité, ces propriétées varient à cause des variations de composition et de température entre r_ζ et l'infini. Cette variation peut être prise en compte si les valeurs de référence sont judicieusement choisies :

$$T_{ref} = (1-a)\,T_\zeta + a T_\infty \tag{B.25}$$

$$Y_{k,ref} = (1-a)\,Y_{k,\zeta} + a Y_{k,\infty} \tag{B.26}$$

où $a = 1/3$ Hubbard et al. [1975], Versaevel [1996].

Traitement numérique de l'ébullition

Le nombre de Spalding de masse (Eq. B.15) présente une singularité quand $Y_{F,\zeta} = 1$. Cette valeur est atteinte quand la température à l'interface atteint la température d'ébullition à la pression considérée $T_b(P)$ donnée par la relation de Clausius-Clapeyron (Eq. B.19) :

$$T_b = \left(\frac{1}{T_{cc}} - \frac{\mathcal{R}}{W_F L_v} \ln\left(\frac{P}{P_{cc}} \right) \right)^{-1} \tag{B.27}$$

Analytiquement la loi d'évaporation (Eq. B.12) ne permet pas d'atteindre la température d'ébullition puisque le flux de chaleur pour le liquide devient nul juste avant. Numériquement, le manque de résolution spatiale ou temporelle peut conduire à des températures supérieures à T_b. Dans ce cas, la température de liquide est fixée à la température d'ébullition et le flux conductif de liquide est fixé à zéro. Le taux d'évaporation est alors :

$$\dot{m}_p \left(T_\zeta = T_b \right) = \frac{\phi_g^c}{\Delta h_{s,F} \left(T_b \right)} \tag{B.28}$$

Valeur de référence pour l'enthalpie liquide

L'enthalpie liquide $h_{s,p}\left(T_\zeta\right)$ est définie à partir d'une valeur de référence différente de celle utilisée pour l'enthalpie du gaz $h_{s,F}\left(T_\zeta\right)$. Il faut donc ajouter un terme additionnel dans l'expression du flux d'enthalpie de la phase liquide : $+\dot{m}_p h_{s,corr}$ avec $h_{s,corr} = h_{s,F}\left(T_{l,ref}\right) - L_v$.

Annexe C

Publications

-A.Vié, L. Martinez, S. Jay, A. Benkenida and B. Cuenot, ***Validation of the eulerian mesoscopic approach in particle-charged homogeneous isotropic decaying turbulence in the scope of large eddy simulation of fuel sprays***, 11^{th} International Conference on Liquid Atomization and Sprays Systems, Vail, USA, 2009

-A.Vié, M. Sanjosé, S. Jay, B. Cuenot, C. Angelberger and M. Massot, ***Evaluation of a multifluid mesoscopic eulerian formalism on the large eddy simulation of an aeronautical-type configuration***, 7^{th} International Conference on Multiphase Flow, Tampa, USA, 2010

ICLASS 2009, 11th Triennial International Annual Conference on Liquid Atomization and Spray Systems, Vail, Colorado USA, July 2009

Validation of the Eulerian Mesoscopic Approach in Particle-Charged Homogeneous Isotropic Decaying Turbulence in the scope of Large Eddy Simulation of Fuel Sprays

A. Vié[*,1], L. Martinez[1], S. Jay[1], A. Benkenida[1] and B. Cuenot[2]
[1]IFP, 1&4 av. de Bois-Préau, 92852 Rueil-Malmaison Cedex - FRANCE
[2]CERFACS, 42 av. G. Coriolis, 31057 Toulouse Cedex 1 - FRANCE

Abstract

This work is devoted to the simulation of Diesel like sprays using an Eulerian-Eulerian approach. For this purpose, the AVBP code is used to perform the computations. It solves the compressible Navier Stokes equations for reactive two phase flows with low dissipation schemes adapted to Large Eddy Simulation (LES). To simulate the liquid phase, the Mesoscopic Eulerian Formalism (MEF) developed by Fevrier et al. is used. In this approach, an analogy is made between particles of a dispersed liquid phase, and molecules in a gas. Starting from the Boltzmann equation, it allows to determine eulerian conservation equations. This formalism was first designed for dilute sprays. In order to simulate fuel sprays in engines, these models have been adapted to dense sprays by the addition of collision effects.

The formalism is validated by Direct Numerical Simulation (DNS) of homogeneous isotropic decaying turbulence, loaded with inertial particles. The carrier phase is initiated with a Passot-Pouquet spectrum. The particles are injected uniformly at the same velocity as the carrier phase.

For non-collisional simulations, results are compared to Eulerian/Lagrangian Discrete Particles Simulation (DPS), considered as a reference. Simulations are performed with one-way coupling drag force (no modification of the gas phase by the liquid phase). As the Stokes number is 1.2, strong preferential concentration effects are expected. Results show that the total energy decrease is well reproduced for both phases with the MEF approach, and that preferential concentration effects are in good agreement with DPS computations.

For collisional simulations, the results are analysed qualitatively. To allow a parametric study, the collision and relaxation time scales of the liquid phase are varied: the Stokes number is varied between 0.6 and 2.4 and the mean liquid volume fraction between 0.027% and 2.7%. Results show that all expected asymptotic behaviours are well exhibited.

Introduction

To simulate fuel sprays, two approaches are commonly used: Lagrangian and Eulerian methods. Lagrangian methods consist in tracking and moving each particles or parcels (group of particles). But for industrial applications, the number of particles required to obtain correct statistics is high and demands multiprocessor computations with efficient load balancing to handle the inhomogeneous dispersed phase.
Eulerian methods are simpler to implement, as they allow to simulate realistic particle concentrations, with the same numerical and parallelization approaches for both gas and liquid phase. However this comes with an increased effort in modeling issues.
This paper is devoted to the validation of the MEF as implemented in AVBP [1] in the case of Homogeneous Isotropic Turbulence (HIT). This validation is done by comparison with DPS performed with the high order NTMIX code [2].

[*]Corresponding author, aymeric.vie@ifp.fr

Equations and models for the dispersed phase

A. Mesoscopic Eulerian Formalism

Eulerian liquid conservation equations are based on the MEF developed by Février et al.[3]. Inspired by the gas kinetic theory, it defines conservation equation, starting from the Boltzmann equation [4].

The key point of this formalism is the decomposition of particle velocities v_p into a correlated part V_p common for all particles, and an uncorrelated part $v'_{p,}$ proper to each particle. After statistical averaging of the particles variables over a large number of realizations, conditioned by one realization of the gas phase, equations for the liquid phase write:

$$\frac{\partial}{\partial t}\rho_l\alpha_l + \frac{\partial}{\partial x_i}\rho_l\alpha_l U_{l,i} = 0 \tag{1}$$

$$\frac{\partial}{\partial t}\rho_l\alpha_l U_{l,i} + \frac{\partial}{\partial x_j}\rho_l\alpha_l U_{l,i}U_{l,j} = \frac{\rho_l\alpha_l}{\tau_p}\left(U_{g,i}-U_{l,i}\right) - \frac{\partial}{\partial x_j}\rho_l\alpha_l\delta R_{l,ij} - \frac{\partial}{\partial x_j}\left(\frac{2}{3}\rho_l\alpha_l\delta\theta_l\delta_{ij} + P_{coll}\delta_{ij}\right) + \frac{\partial}{\partial x_i}\left(\xi_{coll}\frac{\partial}{\partial x_k}U_{l,k}\right) \tag{2}$$

$$\begin{aligned}\frac{\partial}{\partial t}\rho_l\alpha_l\delta\theta_l + \frac{\partial}{\partial x_i}\rho_l\alpha_l\delta\theta_l U_{l,i} &= -2\frac{\rho_l\alpha_l}{\tau_p}\delta\theta_l - \rho_l\alpha_l\delta R_{l,ij}\frac{\partial}{\partial x_j}U_{l,i} - \frac{\partial}{\partial x_j}\rho_l\alpha_l\delta K_{l,iij} \\ &\quad -\left(\frac{2}{3}\rho_l\alpha_l\delta\theta_l + P_{coll}\right)\frac{\partial}{\partial x_j}U_{l,j} + \rho_l\alpha_l\frac{e^2-1}{3\tau_c}\delta\theta_l + \left(\xi_{coll}\frac{\partial}{\partial x_k}U_{l,k}\right)\frac{\partial}{\partial x_i}U_{l,i}\end{aligned} \tag{3}$$

where α_l is the liquid volume fraction, U_l the correlated velocity of the MEF, and $\delta\theta_l$ the Random Uncorrelated discrete particles Energy (RUE) related to the uncorrelated velocity v'_p by the relationship $\delta\theta_l = 1/2.\langle v'_p.v'_p\rangle$. The relaxation time scale is defined as $\tau_p=\rho_l d^2/(18\mu_g)$.

B. Closure Models (with and without collisions)

The equations for the liquid phase presented previously have five unclosed terms : $\delta R_{l,ij}$, $\delta K_{l,iij}$, P_{coll} *and* ξ_{coll}. The two first terms are modeled respectively by a viscous assumption and by a diffusion term similar to Fick's law [5]:

$$\delta R_{l,iij} = -\left(\nu_{kin}+\nu_{coll}\right)\left(\frac{\partial U_{l,i}}{\partial x_j} + \frac{\partial U_{l,j}}{\partial x_i} - \frac{\partial U_{l,k}}{\partial x_k}\frac{\delta_{ij}}{3}\right) \tag{4}$$

$$\delta K_{l,iij} = -\left(\kappa_{kin}+\kappa_{coll}\right)\left(\frac{\partial\delta\theta_l}{\partial x_j}\right) \tag{5}$$

Without collision effects, P_{coll}, ξ_{coll}, ν_{coll} and κ_{coll} are zero, and ν_{kin} and κ_{kin} are written as:

$$\nu_{kin} = \frac{\tau_p}{3}\delta\theta_l, \quad \kappa_{kin} = \frac{10}{27}\tau_p\delta\theta_l \tag{6}$$

Taking into account collision changes the modeling of the kinetic viscosity and diffusion defined in Eq. 6. The principles and development of these models are reviewed in [6],[7]. The collision characteristic time scale is defined as:

$$\tau_c = \frac{d}{24 g_0\alpha_p}\sqrt{\frac{3\pi}{\delta\theta_l}}, \qquad \text{where} \qquad g_0 = \left(1-\frac{\alpha_l}{\alpha_m}\right)^{-2.5\alpha_m} \text{ and } \alpha_m = 0.64 \tag{7}$$

So that the modified kinetic viscosity and diffusivity write:

$$\nu_{kin,c} = \frac{\tau_p}{3}\delta\theta_l\left(1+\alpha_1 g_0\frac{2}{5}(1+e)(3e-1)\right)\Bigg/\left(1+\frac{\tau_p}{\tau_c}\frac{(1+e)(3-e)}{10}\right) \tag{8}$$

$$\kappa_{kin,c} = \frac{2}{3}\delta\theta_l\left(1+\alpha_1 g_0\frac{3}{5}(1+e)^2(2e-1)\right)\Bigg/\left(\frac{9}{5\tau_p}+\frac{(19-33e)(1+e)}{100\tau_c}\right) \tag{9}$$

where e is the elasticity coefficient. ν_{coll}, κ_{coll}, P_{coll} and ξ_{coll} are written as:

$$\nu_{coll} = \frac{4}{5}\alpha_1 g_0 (1+e)\left(\nu_{kin,c} + d\sqrt{\frac{2\delta\theta_l}{3\pi}}\right), \quad \kappa_{coll} = \alpha_1 g_0 (1+e)\left(\frac{6}{5}\kappa_{kin,c} + \frac{4}{3}d\sqrt{\frac{2\delta\theta_l}{3\pi}}\right) \tag{10}$$

$$P_{coll} = \frac{4}{3}\rho_l \alpha_l^2 g_0 (1+e)\delta\theta_l, \quad \xi_{coll} = \frac{4}{3}\rho_l \alpha_l^2 g_0 (1+e) d\sqrt{\frac{2\delta\theta_l}{3\pi}} \tag{11}$$

C. Gas phase equations

Equations for the gas phase are the classical Eulerian Navier-Stokes equations [1]:

$$\frac{\partial}{\partial t}\rho_g + \frac{\partial}{\partial x_i}\rho_g U_{g,i} = 0 \tag{12}$$

$$\frac{\partial}{\partial t}\rho_g U_{g,i} + \frac{\partial}{\partial x_j}\rho_g U_{g,i} U_{g,j} = \frac{\partial}{\partial x_j}\left(-P\delta_{ij} + \tau_{ij}\right) \tag{13}$$

$$\frac{\partial}{\partial t}\rho_g E_g + \frac{\partial}{\partial x_i}\rho_g E_g U_{g,i} = \frac{\partial}{\partial x_j}\left(-P\delta_{ij} + \tau_{ij}\right)U_{g,i} \tag{14}$$

where τ_{ij} is the stress tensor of the gas phase. This set of equation does not take into account the reduction of the gas volume fraction induced by the presence of the liquid phase. Taking into account that the dense zone correspond to a very small region of a spray, this assumption has only a weak influence.

Main characteristics of the HIT test case

The test case is a periodic cubic box sized 2π mm, meshed with 64^3 equivolumes cells. To obtain an initial turbulent gas flow field, a Passot-Pouquet spectrum is used [8]. Particles are uniformly superposed, with the same local velocity as the gas. Fig. 1a shows a gas vorticity field in the median cutting plane. A highly inhomogeneous distribution is observed. The main issue of a gas/particles HIT is that this distribution affects the particles behavior, creating preferential particle concentrations in low vorticity zones, as exhibited by Fig. 1a and Fig. 1b.

To characterize the liquid phase, the Stokes Number is introduced: $St = \tau_p/\tau_L$ where τ_L is the integral Lagrangian time scale of the gas turbulence [9]. As the same gas flow field is used for all cases (turbulence properties are listed in Table 2), the Stokes number only varies with τ_p. Three different values of τ_p were tested, for different liquid loads. Table 3 summarizes the different test cases.

Results and Discussion

All results are presented in non-dimensional variables, denoted by the superscript $^+$. The corresponding reference values are listed in Table 1.

A. Gas HIT

To check the accuracy of AVBP, using a 3rd order scheme, for HIT simulation, the decay of gaseous kinetic energy is compared to the results obtained with NTMIX, and its a 6th order scheme. The results shown in Fig. 2 are in very good agreement, confirming the validity of the AVBP simulation.

B. Gas/particule HIT

Results are analyzed in terms of preferential particle concentration and energy, compared to DPS realized by Kaufmann et al. [10]. As Elghobashi et al. shows in [11], DPS can capture essential features of particles dynamic and may be considered as a reference solution here. Simulations are run in one-way drag coupling. $< . >$ is the averaging operator over the whole domain. The preferential particle concentration is evaluated by a distribution function [12]:

$$g_{pp}^{\Delta x} = < n_p^2(\vec{x}) > / < n_p(\vec{x}) >^2 \tag{15}$$

A first test case is carried out to verify the MEF. The Stokes number is set to 1.2. Fig. 3 compares the different energy terms for both approaches (MEF and DPS) and the agreement is very good. For a better view, the uncorrelated

energy is plotted again in Fig. 4, showing a very accurate prediction of the MEF. This demonstrates the excellent behavior of the closure models for RUE terms, defined previously. Figure 5 shows the preferential particle concentration and again the good performance of MEF, compared to DPS.
Considering collisional simulations, results are analyzed qualitatively only. Figures 6 and Fig. 7 show the results for MEF simulations without collisions, then with collisions for two different loads. Preferential particle concentration and RUE both show that the model degenerates to the non-collisionnal case when the liquid volume fraction goes to 0. Furthermore, collisions increase the preferential particle concentration effect and decrease RUE. As explained by Fede et al. [13], the first effect is due to the diminution of the mean free path of the particles, acting as a the diminution of the liquid phase viscosity [14]. Concerning RUE, considering that the total energy of the particles is not affected by collisions, the effect may be only due to a modification of the energy exchange between correlated and uncorrelated motions.
To qualify the influence of the Stokes number time, the relaxation time is modified trough the liquid density. Figures 8 and Fig. 9 preferential concentration and RUE for the three cases. For lower τ_p, collisions have no effect, even with high volume fractions. When increasing τ_p, collisions effects on preferential particle concentration and RUE become more and more sensible and predominant.

Conclusions

An extension to dense sprays of the Mesoscopic Eulerian Formalism (MEF) is presented and validated. First it is shown how the MEF compares with DPS approach in the particular test case of HIT with a diluted dispersed phase.
Very good agreement is obtained in terms of energy and preferential particles concentration. In particular, the fact that total energy evolution is perfectly reproduced is very important, and demonstrates that the formalism represents the one-way drag coupling very well, without loss of energy.
This allows to add collisions and run MEF simulations to study the effects on the dispersed phase. Expected asymptotic behaviors are well exhibited, with degeneracy to non-colliding results for small liquid volume fractions.
The next step is to compare MEF results to DPS results with collisions and two-way coupling, and to investigate the importance of polydispersion (in terms of droplet diameter and velocity) in the same configuration.

Acknowledgment

Numerical computations of the Eulerian simulations were performed on the supercomputer of IFP. The authors wish to thank Dr E. Riber and Dr P. Fede for many fruitful discussions.

Nomenclature

e inelasticity coefficient
E total enthalpy
g_{pp} distribution function
n_p number of particles
U velocity
α_l liquid volume fraction
$\delta\theta_l$ random uncorrelated energy
κ diffusivity
ν viscosity
τ_c collision rate
τ_L integral time scale
τ_p relaxation time scale

Subscripts
g gas
l liquid
kin kinetic
coll collisional

Superscripts
+ adimensioned variable

References

1. Moureau, V., Lartigue, G., Sommerer, Y., Angelberger, C., Colin, O., and Poinsot, T., *Journal of Computational Physics* 202: 710-736 (2005).
2. Vermorel, O., Bédat,B., Simonin, O., and Poinsot, T., *Journal of Turbulence* 335: 75-109 (2003).
3. Février, P., Simonin, O., and Squires, K., *Journal of Fluid Mechanics* 533: 1-46 (2005).
4. Chapman, S., and Cowling, T., *The mathematical theory of non-uniform gazes*, Cambridge University Press, 1939.
5. Kaufmann, A. Simonin, O., and Poinsot, T., *5th International Conference on Multiphase Flow*, Yokohama, Japan, 2005.
6. Peirano, E., and Leckner, B., *Progress in Energy and Combustion Science* 24: 259-296 (1996).
7. Boelle, A., Blazer, G., and Simonin, O., *Sixth ASME Gas-Solid Flows Symposium*, Hilton Head Island, US, 1995.
8. Passot, T., and Pouquet, A., *Journal of Fluid Mechanics* 181: 441-466 (1987).
9. Hogan, R.C., Cuzzi, J.N., *Physics of Fluids* 13: 2938-2945 (2001).

10. Kaufmann, A., Moreau, M., Simonin, O., and Hélie, J., *Journal of Computational Physics* 227: 6448-6472 (2008).
11. Elghobashi, S. and Truesdell, G., *Journal of Fluid Mechanics* 242: 655-700 (1992).
12. Simonin, O., Zaichik, L.I., Alipchenkov, V.M., and Février, P., *Physics of Fluids* 18: 125107 (2006).
13. Fede, P., and Simonin, O., *Physics of Fluids* 18: 045103 (2006).
14. Martinez, L., Benkenida, A., and Cuenot, B., *21th ILASS – Europe Meeting*, Muğla, Turkey, 2007.

Table 1. References variables.

L_{ref} (m)	t_{ref} (s)	U_{ref} ($m.s^{-1}$)	μ_{ref} ($kg.m^{-1}.s^{-1}$)
10^{-3}	$2.8818\ 10^{-6}$	347.0	$2.02\ 10^{-3}$

Table 2. Gas phase properties.

$u_f'^+$	ε^+	Re_t	l_t^+	η^+	τ_L^+	τ_η^+
0.0781	0.001	12.95	0.81	0.10	4.30	2.16

Table 3. Liquid phase properties for collisional and non-collisional cases.

α_l	St	τ_p^+	ρ_l ($kg.m^{-3}$)	d_l (μm)
0.00027	1.2	5.47	1916	17.3
0.027	1.2	5.47	1916	17.3
0.027	0.6	2.73	958	17.3
0.027	2.4	10.94	3832	17.3

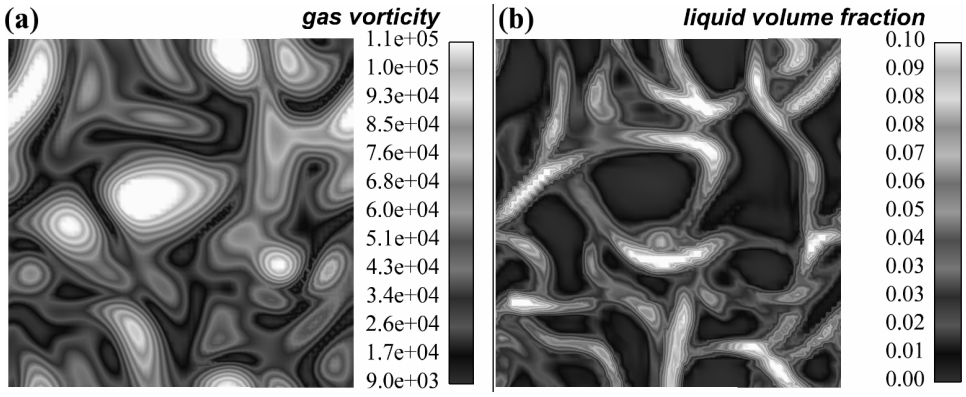

Figure 1. HIT (median cutting plane): (a) gas vorticity; (b) liquid volume fraction.

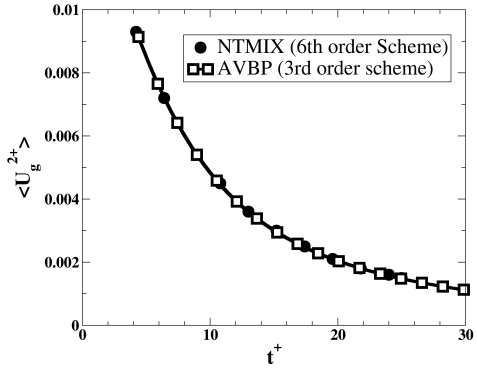

Figure 2. Gaseous kinetic energy time evolution: AVBP simulation (squares), NTMIX simulation.

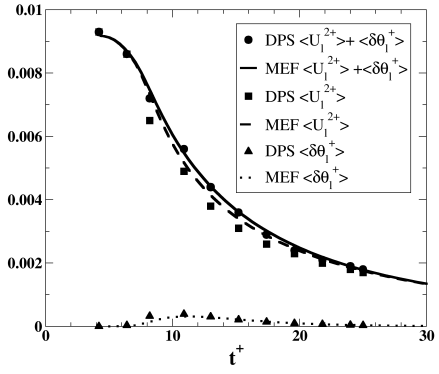

Figure 3. Liquid mean energies time evolution: total energy from DPS (circles) and MEF (solid line); correlated energy from DPS (squares) and MEF (dashed line); RUE from DPS (triangle up) and MEF (dotted line).

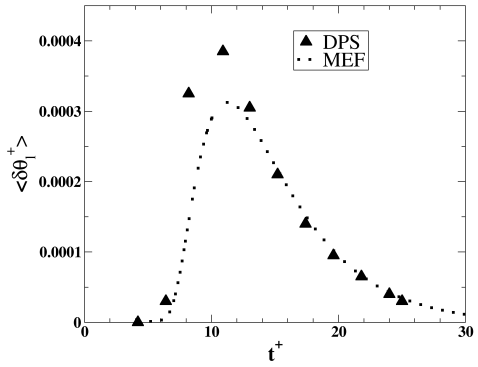

Figure 4. Mean RUE time evolution: MEF simulation (dots), DPS simulation (triangles).

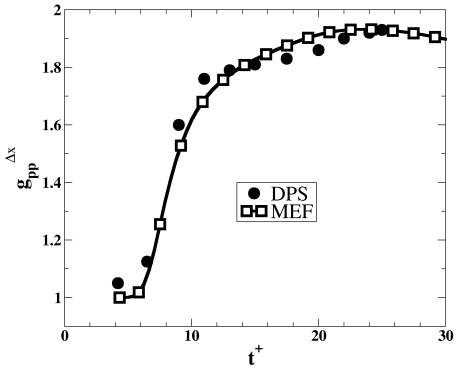

Figure 5. Preferential particle concentration time evolution: MEF simulation (squares), DPS simulation (circles).

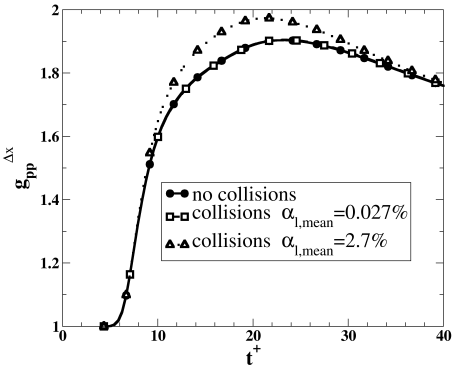

Figure 6. Preferential particle concentration time evolution of MEF simulations: without collisions (circle), with collisions at $\alpha_{l,mean}=0.027\%$ (square), with collisions at $\alpha_{l,mean}=2.7\%$ (triangle up).

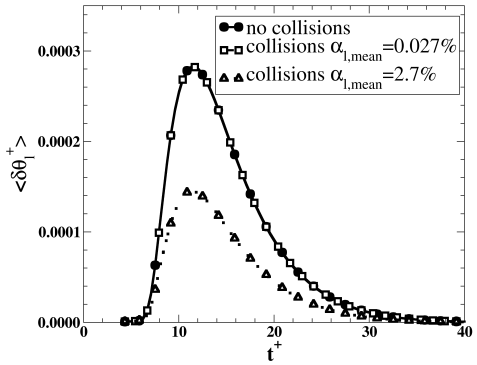

Figure 7. Mean RUE time evolution of MEF simulations: without collisions (circle), with collisions at $\alpha_{l,mean}=0.027\%$ (square), with collisions at $\alpha_{l,mean}=2.7\%$ (triangle up).

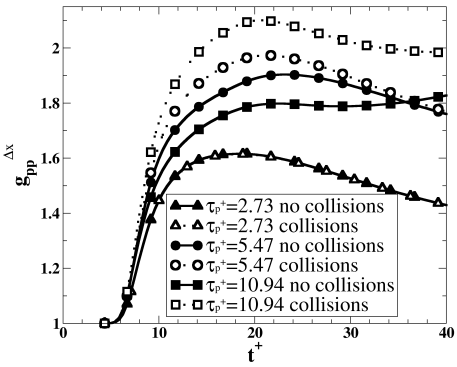

Figure 8. Preferential particle concentration time evolution of MEF simulations: with (full symbols) and without collisions (empty symbols); $\tau_p^+=2.73$ (triangles up), $\tau_p^+=5.47$ (circles) and $\tau_p^+=10.94$ (squares).

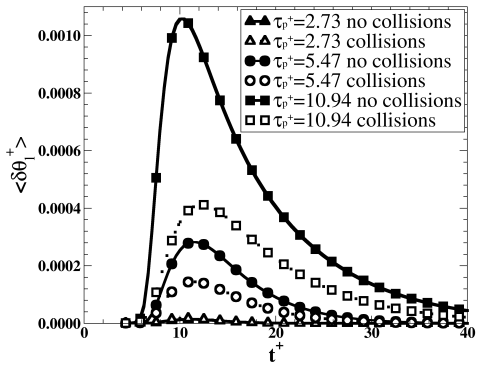

Figure 9. Mean RUE time evolution of MEF simulations: with (full symbols) and without collisions (empty symbols); $\tau_p^+=2.73$ (triangles up), $\tau_p^+=5.47$ (circles) and $\tau_p^+=10.94$ (squares).

7th International Conference on Multiphase Flow,
ICMF 2010, Tampa, FL, May 30 – June 4, 2010

Evaluation of a Multifluid Mesoscopic Eulerian Formalism on the Large Eddy Simulation of an aeronautical-type configuration

A. Vié*, M. Sanjosé†, S. Jay*, C. Angelberger*, B. Cuenot† and M. Massot‡

* IFP, 1&4 av. de Bois Préau, 92852 Rueil-Malmaison Cedex, FRANCE

† CERFACS, 42 av. G. Coriolis, 31057 Toulouse Cedex 1, FRANCE

‡ EM2C, CNRS UPR288, École Centrale de Paris, 92295 Châtenay-Malabry, FRANCE

aymeric.vie@ifp.fr

Keywords: Large Eddy Simulation, Two-phase flow, Eulerian Mesoscopic, Multifluid, aeronautical swirl injector

Abstract

This work describes the evaluation of a fully eulerian method to simulate polydisperse turbulent two phase flows: the Multifluid Mesoscopic Eulerian Formalism (MMEF). This approach is derived from the coupling between the Mesoscopic Eulerian Formalism (MEF) of Février et al. (2005), and the Multifluid Approach (MA) of Laurent and Massot (2001). The MA handles polydispersion by using a discretization of the droplet size space, whereas the MEF describes the velocity dispersion of monodisperse turbulent particle flows. The coupling of the two methods is expected to capture both behaviors. A first step toward this kind of approach was initially studied in Massot (2007), and the differences with the present work lie in the closure and modelling assumptions.
MMEF is integrated into the AVBP code from CERFACS/IFP, which solves the compressible Navier-Stokes equations for reactive flows with low dissipation schemes adapted to Large Eddy Simulation. These schemes encounter some difficulty for the Eulerian description of the liquid dispersed spray, highly compressible and showing stiff gradients and vacuum areas of droplet density. Specific numerical procedures are used to stabilize locally the solution, with limited effect on the accuracy.
The model is applied to the MERCATO aeronautical-type configuration. An analysis of characteristic time scales allows to evaluate the importance of polydispersion in this test rig. A preliminary test case consists in the evaporation of a chosen distribution in one computational cell. Physical conditions are the same as in MERCATO. Results are compared to the evaporation strategy used with MEF, and show the necessity to account for polydispersion description in order to capture size-velocity correlations.
A second test case is a two-dimensional vortex entraining droplets, in which droplets are injected uniformly. Due to the polydispersion of the liquid and its resulting centrifugal force, a spatial distribution of droplet mean diameter is observed, and confirms again the necessity of polydispersion.
Finally, the MMEF is applied to the MERCATO test rig, for which both experimental and numerical data are available. Comparisons of velocity profiles at selected downstream positions show a good agreement with measurements of MEF and MMEF in the central zone, whereas only the MMEF is able to capture the external zone. Comparisons of Droplet Number Density function at selected volumes inside the chamber also show a good agreement between MMEF and experiments.

Nomenclature

Roman symbols

c_p	droplet velocity ($\mathrm{m.s^{-1}}$)
f_p	Number Density Function
N	number of sections
S	droplet surface ($\mathrm{m^2}$)
D	deformation tensor ($\mathrm{s^{-1}}$)
T	droplet temperature (K)
u	phase velocity

Greek symbols

μ	kinetic viscosity ($\mathrm{m^2.s^{-1}}$)
ρ	density ($\mathrm{kg.m^{-3}}$)
τ_p	relaxation time (s)
Θ_l	Random Uncorrelated Energy ($\mathrm{m^2.s^{-2}}$)

Subscripts

g	gas
l	liquid
p	particle

Superscripts

(p)	section p

Others

δc_p	uncorrelated droplet velocity ($\mathrm{m.s^{-1}}$)
$\delta \mathbf{R_l}$	2nd order velocity correlations tensor ($\mathrm{m^2.s^{-2}}$)
$\delta \mathbf{S_l}$	3rd order velocity correlations tensor ($\mathrm{m^3.s^{-3}}$)
$\widehat{.}$	Favre averaged quantity
$\bar{.}$	Reynolds averaged quantity

Introduction

Large Eddy Simulation (LES) is a promising tool to improve the prediction of the mixture inside aeronautical combustion chambers. Indeed, its ability to solve a wide range of the turbulence spectrum, modelling only the smallest scales, allows to reproduce more accuratly interactions between the turbulence and the liquid fuel droplets.

This work aims at evaluating performance for liquid injection inside an aeronautical combustor. Lagrangian particle tracking methods are classically used but they suffer from numerical issues (parallelisation, statistical convergence, high number of particles) and special care must be taken for the liquid/gas coupling problems (interpolation of gas velocity, distribution of liquid/gas source terms)(Garcia (2009)). An alternative is eulerian methods, which use the same numerical methods for the gas and the liquid phases, and can be efficiently parallelized. So it seems well suited for complex industrial applications. However, it raises a number of modelling issues. In particular, the modelling of polydispersion is a difficult question. The Mesoscopic Eulerian Formalism (MEF)(Février et al. (2005)) is based on a locally monodisperse assumption, so it has no particle size distribution. To tackle this problem, the Multifluid Approach (MA) of Laurent and Massot (2001) has been coupled with the MEF. This formalism, called Multifluid Mesoscopic Eulerian Formalism (MMEF), is integrated in the AVBP code. After presenting the model equations and preliminary test cases, MMEF is applied to an aeronautical-type configuration. This application was simulated with lagrangian and eulerian methods (Sanjosé et al. (2008)), but never with a polydisperse eulerian formalism.

Model equations

The MEF is a statistical approach based on the droplet number density function (NDF) f_p:

$$f_p = f_p(\mathbf{x}, t, \mathbf{c_p}, S, T) \tag{1}$$

where t, $\mathbf{x}$, $\mathbf{c_p}$, S, T are respectively the time, droplet position, velocity, surface and temperature. The evolution of this NDF is driven by a Williams-Boltzmann equation (WBE) (Williams (1958)):

$$\frac{\partial f_p}{\partial t} + \frac{\partial c_{p,j} f_p}{\partial x_j} + \frac{\partial F_{d,j} f_p}{\partial c_{p,j}} + \frac{\partial R_S f_p}{\partial S} + \frac{\partial E_T f_p}{\partial T} = 0 \tag{2}$$

where $\mathbf{F}_d$, R_S and E_T correspond to drag force, mass and heat transfer. The drag force F_d is written as :

$$\mathbf{F}_d = \frac{\mathbf{c_p} - \mathbf{u_{g@l}}}{\tau_p} \tag{3}$$

where $\mathbf{u}_{g@l}$ is the gas velocity at droplet position, and $\tau_p = \rho_l S/18\pi\mu_g$ is the particle relaxation time. R_S and E_Θ are defined as:

$$R_S = \frac{dS}{dt} = \frac{4\sqrt{\pi}}{\rho_l S^{1/2}} \dot{m}_p \tag{4}$$

$$E_T = \frac{dT}{dt} = \frac{Q_p}{m_p C_{p,l}} \tag{5}$$

where $\dot{m}_p$ is the mass rate, and Q_p is the heating flux. Those source terms are modeled using a finite liquid conductivity with a gas spherical symmetry diffusion model (Kuo (2005), Sirignano (1999)).

Using $< \Phi >= 1/n_l \int_{\mathbb{R}} \Phi f_p dc_p dT$ as an averaging

operator, some characteristic quantities are defined:

$$\begin{aligned} n_l(x,t,S) &= \int_{\mathbb{R}} f_p dc_p dT \\ u_{l,i}(x,t,S) &= < c_{p,i} > \\ T_l(x,t,S) &= < T > \\ \delta c_{p,i}(x,t,S) &= c_{p,i} - u_{l,i} \\ \delta R_{l,ij}(x,t,S) &= < \delta c_{p,i} \delta c_{p,j} > \\ \delta\Theta_l(x,t,S) &= \delta R_{l,ii}(x,t,S)/2 \\ \delta S_{l,ijk}(x,t,S) &= < \delta c_{p,i} \delta c_{p,j} \delta c_{p,k} > \end{aligned}$$

where $u_{l,i}$ is the mesoscopic eulerian velocity field, shared by all particles of size S at position x and time t and δc_p is a residual velocity, proper to each particle. T_l, $\delta R_{l,ij}$, $\delta S_{l,ijk}$ and $\delta\Theta_l$ are respectively the liquid mean temperature, the second and third order velocity correlation tensors, and the Random Uncorrelated Energy (RUE), corresponding to the residual velocity.

Multiplying the WBE (Eq. 2) by any function Ψ, and integrating over particles velocities and temperatures, one can obtain the equation of Enskog:

$$\begin{aligned} &\frac{\partial}{\partial t} n_l \langle\Psi\rangle + \frac{\partial}{\partial x_j} n_l u_{l,j} \langle\Psi\rangle + \frac{\partial}{\partial S} n_l \langle R_S \Psi\rangle = \\ &\quad + n_l \langle F_{d,j} \frac{\partial \Psi}{\partial c_{p,j}}\rangle + n_l \langle R_S \frac{\partial \Psi}{\partial S}\rangle + n_l \langle E_T \frac{\partial \Psi}{\partial T}\rangle \\ &\quad + n_l \langle \frac{\partial \Psi}{\partial t}\rangle + n_l \langle c_{p,j} \frac{\partial \Psi}{\partial x_j}\rangle + \frac{\partial}{\partial x_j} n_l \langle \delta c_{p,j} \Psi\rangle \end{aligned} \tag{6}$$

Replacing Ψ by target quantities, the semi-kinetic system (Laurent et al. (2004)) is obtained:

$$\frac{\partial}{\partial t} n_l + \frac{\partial}{\partial x_m} n_l u_{l,m} = -\frac{\partial}{\partial S} n_l R_S \tag{7}$$

$$\begin{aligned} &\frac{\partial}{\partial t} n_l u_{l,i} + \frac{\partial}{\partial x_m} n_l u_{l,i} u_{l,m} = -\frac{\partial}{\partial S} n_p u_{l,i} R_S \\ &\quad - \frac{n_l}{\tau_p} (u_{l,i} - u_{g,i}) - \frac{\partial}{\partial x_m} n_l \delta R_{l,im} \end{aligned} \tag{8}$$

$$\begin{aligned} &\frac{\partial}{\partial t} n_l \Theta_l + \frac{\partial}{\partial x_m} n_l \Theta_l u_{l,m} = -\frac{\partial}{\partial S} n_l \Theta_l R_S \\ &\quad - 2\frac{n_l}{\tau_p}\Theta_l - n_l \delta R_{l,ij} \frac{\partial}{\partial x_j} u_{l,i} - \frac{\partial}{\partial x_j} n_l \delta S_{l,iij} \end{aligned} \tag{9}$$

$$\frac{\partial}{\partial t} n_l H_l + \frac{\partial}{\partial x_m} n_l H_l u_{l,m} = -\frac{\partial}{\partial S} n_l R_S H_l + n C_{p,l} E_T \tag{10}$$

where $H_l = C_p T_l$ is the liquid enthalpy. The approach described here is similar to the one used in Reveillon et al. (2002) and Massot (2004), as they start from a decomposition into mean and uncorrelated velocities, but differences appear when the uncorrelated terms are closed.

To obtain the multi-fluid system, the semi-kinetic system (Eq. 7-10) is integrated over particule size, assuming a discretization in N intervals $[S_p, S_{p+1}]$ called section from Greenberg et al. (1993): superscript (p) designates mass-weighted averaged quantities in interval p. Sectionnal quantities are then defined:

$$n_l(x,t,S) = m_l^{(p)}(x,t)\kappa_S^{(p)}(S) \tag{11}$$

$$m_l^{(p)}(x,t) = \int_{S_p}^{S_{p+1}} \rho_l \frac{S^{3/2}}{6\sqrt{\pi}} n_l dS \tag{12}$$

where $\kappa_S^{(p)}(S)$ is the shape of the distribution function over each section. Multiplying the kinetic system (Eq. 7-10) by $\rho_l \frac{S^{3/2}}{6\sqrt{\pi}}$ and integrating over sections gives:

$$\frac{\partial}{\partial t} m_l^{(p)} + \frac{\partial}{\partial x_m} m_l^{(p)} u_{l,m}^{(p)} = E^{(p)}(1) \tag{13}$$

$$\begin{aligned} &\frac{\partial}{\partial t} m_l^{(p)} u_{l,i}^{(p)} + \frac{\partial}{\partial x_m} m_l^{(p)} u_{l,i}^{(p)} u_{l,m}^{(p)} = E^{(p)}(u_{l,i}^{(p)}) \\ &\quad - \frac{m_l^{(p)}}{\tau_p^{(p)}} \left(u_{l,i}^{(p)} - u_{g,i}\right) - \frac{\partial}{\partial x_m} m_l^{(p)} \delta R_{l,im}^{(p)} \end{aligned} \tag{14}$$

$$\begin{aligned} &\frac{\partial}{\partial t} m_l^{(p)} \delta\Theta_l^{(p)} + \frac{\partial}{\partial x_m} m_l^{(p)} \delta\Theta_l^{(p)} u_{l,m}^{(p)} = E^{(p)}(\delta\Theta_l^{(p)}) \\ &\quad - 2\frac{m_l^{(p)}}{\tau_p^{(p)}} \delta\Theta_l^{(p)} + \Xi^{(p)} \end{aligned} \tag{15}$$

$$\begin{aligned} &\frac{\partial}{\partial t} m_l^{(p)} H_l^{(p)} + \frac{\partial}{\partial x_m} m_l^{(p)} H_l^{(p)} u_{l,m}^{(p)} = E^{(p)}(H_l^{(p)}) \\ &\quad + m_l^{(p)} C_{p,l} E_T^{(p)} \end{aligned} \tag{16}$$

where $E^{(p)}(\Phi)$ is the evaporation source term defined as:

$$\begin{aligned} E^{(p)}(\Phi^{(p)}) = &- \left(E_1^{(p)} + E_2^{(p)}\right) m_l^{(p)} \Phi^{(p)} \\ &+ E_1^{(p+1)} m_l^{(p+1)} \Phi^{(p+1)} \end{aligned} \tag{17}$$

and $\Xi^{(p)}$ is the uncorrelated flux of $\delta\Theta_l^{(p)}$ defined as:

$$\Xi^{(p)} = - m_l^{(p)} \delta R_{l,ij}^{(p)} \frac{\partial}{\partial x_j} u_{l,i}^{(p)} - \frac{\partial}{\partial x_m} m_l^{(p)} \delta S_{l,iim}^{(p)} \tag{18}$$

In Massot (2004), $\delta S_{l,iim}^{(p)}$ is neglected, whereas only the isotropic part of $\delta R_{l,ij}^{(p)}$ is considered in Eq. 14 and Eq. 18. For the isotropic test cases studied in Massot (2004), these assumptions have been verified by eulerian filtering of lagrangian computations. In the final application studied here, it is not possible to use these assumptions, due to the anisotropy of shear flows. So

the uncorrelated flux $\delta R_{l,ij}^{(p)}$ is decomposed into spherical and deviatoric parts:

$$\delta R_{l,ij}^{(p)} = P_{RUM}^{(p)}\delta_{ij} + \delta\Sigma_{l,ij}^{(p)} \tag{19}$$

where $P_{RUM}^{(p)} = 2/3\widehat{\delta\Theta}_l^{(p)}$ is the pressure due to Random Uncorrelated Motion. $\delta\Sigma_{l,ij}^{(p)}$ and $\delta S_{l,iim}^{(p)}$are closed using respectively a viscous assumption and a diffusion term similar to Fick's law (Kaufmann et al. (2008)):

$$\delta\Sigma_{l,ij}^{(p)} = -\nu_{RUM}^{(p)} D_{l,ij}^{(p)} \tag{20}$$

$$\delta S_{l,iim}^{(p)} = -\kappa_{RUM}^{(p)} \frac{\partial\delta\Theta_l^{(p)}}{\partial x_m} \tag{21}$$

where $D_{l,ij}^{(p)} = \left(\frac{\partial u_{l,i}^{(p)}}{\partial x_j} + \frac{\partial u_{l,j}^{(p)}}{\partial x_i} - \frac{\partial u_{l,k}^{(p)}}{\partial x_k}\frac{\delta_{ij}}{3}\right)$, $\nu_{RUM}^{(p)} = \tau_p^{(p)}\delta\Theta_l^{(p)}/3$, and $\kappa_{RUM}^{(p)} = 2\Theta_l^{(p)}/3$. Those closures are derived from the assumption of a velocity distribution close to the maxwellian equilibrium one, which has been validated on Homogeneous Isotropic Turbulence for low Stokes Number (Vié et al. (2009)). But its validity for high Stokes numbers or shear flows is quite questionable, because the near-equilibrium assumption would not be verified. This issue is investigated in Masi (2010). It is shown that the anisotropy of the shear stress has to be accounted for.

As proposed in de Chaisemartin (2009) and advised in Laurent (2006), a distribution constant in radius is chosen. The function $\kappa_S^{(p)}(S)$ is then:

$$\kappa_S^{(p)}(S) = \frac{12}{\rho_l(S_{p+1}^2 - S_p^2)}\sqrt{\frac{\pi}{S}} \tag{22}$$

Evaporation terms are derived by an integration by part $\int_{S_p}^{S_{p+1}} \rho_l S^{3/2}/(6\sqrt{\pi}) R_S n_l dS$ (de Chaisemartin (2009)):

$$E_1^{(p)} = \rho_l \frac{S_p^{3/2}}{6\sqrt{\pi}} R_S^{(p)}\kappa_S^{(p)} = \frac{2S_p}{S_{p+1}^2 - S_p^2} R_S^{(p)} \tag{23}$$

$$E_2^{(p)} = \int_{S_p}^{S_{p+1}} \rho_l \frac{d_S(S^{3/2})}{6\sqrt{\pi}} R_S n_l dS = \frac{3}{S_p + S_{p+1}} R_S^{(p)} \tag{24}$$

where $E_1^{(p)}$ is the mass exchange between sections, and $E_2^{(p)}$ is the mass exchange with the gas phase.

Gas phase equations are the classical Navier-Stokes equations, with the coupling terms between liquid and gas phases due to drag and evaporation. As the liquid volume fraction is very low in the final application, the volume occupied by the liquid is neglected:

$$\frac{\partial}{\partial t}\rho_g + \frac{\partial}{\partial x_m}\rho_g u_{g,m} = \sum_{p=1}^{N} E_2^{(p)} m_l^{(p)} \tag{25}$$

$$\frac{\partial}{\partial t}\rho_g u_{g,i} + \frac{\partial}{\partial x_m}\rho_g u_{g,i}u_{g,m} = -\frac{\partial P}{\partial x_i} + \frac{\partial}{\partial x_m}\rho_g\nu_g D_{g,im} + \sum_{p=1}^{N}\left(\frac{m_l^{(p)}}{\tau_p^{(p)}}\left(u_{l,i}^{(p)} - u_{g,i}\right) + E_2^{(p)} m_l^{(p)} u_{l,i}^{(p)}\right) \tag{26}$$

$$\frac{\partial}{\partial t}\rho_g E_g + \frac{\partial}{\partial x_m}(\rho_g E_g + P)u_{g,m} = + \frac{\partial}{\partial x_m}\rho_g\nu_g D_{g,im}u_{g,i} + \frac{\partial}{\partial x_m}Q_{g,ij} + \sum_{p=1}^{N}\begin{pmatrix} E_2^{(p)} m_l^{(p)} u_{g,i}u_{l,i}^{(p)} - m_l^{(p)} C_{p,l} E_T^{(p)} \\ + \frac{m_l^{(p)}}{\tau_p^{(p)}}\left(u_{l,i}^{(p)} - u_{g,i}\right)u_{g,i} \end{pmatrix} \tag{27}$$

where E_g is the total energy and $Q_{g,ij}$ is the heat flux.

In the LES approach, liquid and gas equations are filtered through a Favre averaging procedure (Moreau et al. (2010)). The resulting set of equations for the liquid phase is:

$$\frac{\partial}{\partial t}\overline{m}_l^{(p)} + \frac{\partial}{\partial x_m}\overline{m}_l^{(p)}\widehat{u}_{l,m}^{(p)} = \widehat{E}^{(p)}(1) \tag{28}$$

$$\frac{\partial}{\partial t}\overline{m}_l^{(p)}\widehat{u}_{l,i}^{(p)} + \frac{\partial}{\partial x_m}\overline{m}_l^{(p)}\widehat{u}_{l,i}^{(p)}\widehat{u}_{l,m}^{(p)} = \widehat{E}^{(p)}(u_{l,i}^{(p)}) - \frac{\overline{m}_l^{(p)}}{\tau_p}\left(\widehat{u}_{l,i}^{(p)} - \widehat{u}_{f@l,i}\right) + \Omega_i^{(p)} \tag{29}$$

$$\frac{\partial}{\partial t}\overline{m}_l^{(p)}\widehat{\delta\Theta}_l^{(p)} + \frac{\partial}{\partial x_m}\overline{m}_l^{(p)}\widehat{\delta\Theta}_l^{(p)}\widehat{u}_{l,m}^{(p)} = \widehat{E}^{(p)}(\delta\Theta_l^{(p)}) - 2\frac{\overline{m}_l^{(p)}}{\tau_p}\widehat{\delta\Theta}_l^{(p)} + \widehat{\Xi}^{(p)} \tag{30}$$

$$\frac{\partial}{\partial t}\overline{m}_l^{(p)}\widehat{H}_l^{(p)} + \frac{\partial}{\partial x_m}\overline{m}_l^{(p)}\widehat{H}_l^{(p)}\widehat{u}_{l,m}^{(p)} = \widehat{E}^{(p)}(H_l^{(p)}) + \overline{m}_l^{(p)} C_{p,l} E_T^{(p)} \tag{31}$$

where $\Omega_i^{(p)}$ and $\widehat{\Xi}^{(p)}$ are defined as:

$$\Omega_i^{(p)} = -\frac{\partial}{\partial x_m}\overline{m}_l^{(p)}\delta\widehat{R}_{l,im}^{(p)} - \frac{\partial}{\partial x_m}\overline{m}_l^{(p)}T_{l,im}^{(p)} \tag{32}$$

$$\widehat{\Xi}^{(p)} = -\overline{m}_l^{(p)}\left(\widehat{\delta R}_{l,ij}^{(p)} + T_{l,ij}^{(p)}\right)\frac{\partial}{\partial x_j}\widehat{u}_{l,i}^{(p)} - \frac{\partial}{\partial x_m}\overline{m}_l^{(p)}\widehat{\delta S}_{l,iim}^{(p)} \tag{33}$$

where $T_{l,ij}^{(p)}$ is the subgrid scale tensor modeled using a Smagorinski-Yoshizawa model (Moreau et al. (2010)). The resulting set of equations for the gas phase is:

$$\frac{\partial}{\partial t}\rho_g + \frac{\partial}{\partial x_m}\rho_g \widehat{u}_{g,m} = \sum_{p=1}^{N} E_2^{(p)} \overline{m}_l^{(p)} \tag{34}$$

$$\begin{aligned}\frac{\partial}{\partial t}\rho_g \widehat{u}_{g,i} + \frac{\partial}{\partial x_m}\rho_g \widehat{u}_{g,i}\widehat{u}_{g,m} = \\ - \frac{\partial \widehat{P}}{\partial x_i} + \frac{\partial}{\partial x_m}\rho_g \nu_g \widehat{D}_{g,im} + \frac{\partial}{\partial x_m} T_{g,ij} \\ + \sum_{p=1}^{N}\left(\frac{\overline{m}_l^{(p)}}{\overline{\tau}_p^{(p)}}\left(\widehat{u}_{l,i}^{(p)} - \widehat{u}_{g,i}\right) + E_2^{(p)}\overline{m}_l^{(p)}\widehat{u}_{l,i}^{(p)}\right)\end{aligned} \tag{35}$$

$$\begin{aligned}\frac{\partial}{\partial t}\rho_g \widehat{E}_g + \frac{\partial}{\partial x_m}(\rho_g \widehat{E}_g + \widehat{P})\widehat{u}_{g,m} = \\ + \frac{\partial}{\partial x_m}\rho_g \nu_g \widehat{D}_{g,im}\widehat{u}_{g,i} + \frac{\partial}{\partial x_m}\overline{Q}_{g,ij} \\ + \sum_{p=1}^{N}\begin{pmatrix} E_2^{(p)}\overline{m}_l^{(p)}\widehat{u}_{g,i}\widehat{u}_{l,i}^{(p)} - \overline{m}_l^{(p)} C_{p,l} E_T^{(p)} \\ + \frac{\overline{m}_l^{(p)}}{\overline{\tau}_p^{(p)}}\left(\widehat{u}_{l,i}^{(p)} - \widehat{u}_{g,i}\right)\widehat{u}_{g,i}\end{pmatrix}\end{aligned} \tag{36}$$

where $T_{g,ij}$ is the subgrid scale tensor modeled using the WALE model (Nicoud et Ducros (1999)).

Numerical Context in the AVBP Code

The AVBP code solves compressible Navier-Stokes equation for reactive flows on unstructured grids in a cell-vertex formulation. To perform Large Eddy Simulations, a 3^{rd} order in time and space scheme is used (TTGC)(Colin et al. (2000)).

The eulerian liquid phase is similar to the eulerian gas phase in terms of equations, but has different behaviours. It is highly compressible, so that vacuum and strong gradients occurs. As the TTGC scheme doesn't preserve positivity, it encounters difficulties in such zones. A classical way to handle such numerical problems is to use artificial viscosity. This methodology has been applied to the simulation of a decaying Homogeneous Isotropic Turbulence (Vié et al. (2009)), and seems to be very accurate. However more adapted schemes are needed, like kinetic schemes in de Chaisemartin (2009). But their adaptation to unstructured cell vertex 3-dimensional formulation is not straightforward and requires important developments.

The MERCATO test rig

The test rig is an experimental swirl combustor (Fig. 1). Air is injected inside the plenum and enters the combustion chamber through the swirler. The liquid injection is located at the end of the swirler stage, and at the center of the swirled gaseous jet. The case studied is a two-phase evaporating flow without combustion. Pressure and temperature of the gas phase are 1bar and 463K. Experimental data obtained by PDA and LDA is available (Garcia-Rosa (2008)).

The injection system is a pressure-swirl atomizer. It generates a hollow cone spray with an half angle of $40°$ and orthoradial motion, which produces a polydisperse cloud of droplets. The NDF at 13mm downstream the injector is shown in Fig. 2. The injected fuel is a surrogate for kerosene JP10 for which thermodynamic and transport properties are taken from Boileau (2007).

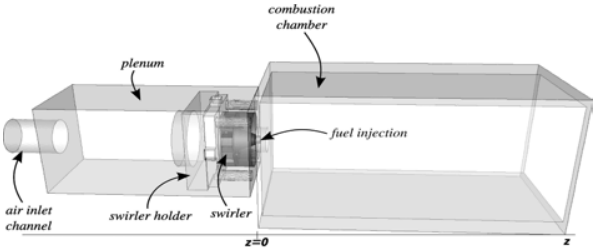

Figure 1: Scheme of the MERCATO test rig.

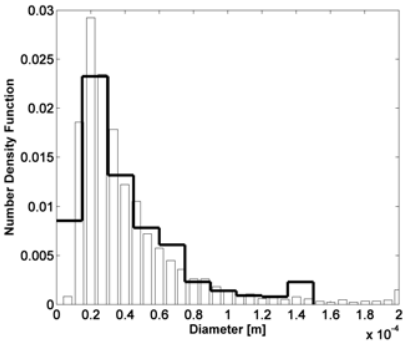

Figure 2: MERCATO: Number Density Function at 13mm downstream the injector location (histogram) and Multifluid representation with 10 sections (solid line).

Preliminary test cases

As evaporation modifies droplets size, it is a good test for a multifluid approach. Such test case was already

studied in Laurent (2006), Dufour et al. (2005), or de Chaisemartin (2009). The same evaporation conditions as in the MERCATO are used. Because of heating, no analytical solution is available but MEF and MMEF are compared. For MEF, the droplet distribution is reduced to a Dirac distribution around the mean diameter which evolves in time. For MMEF, the initial droplet distribution is discretized in sections, as shown on Fig. 2. The initial mean diameter (d10) is $55\mu m$. Figure 3 shows the time evolution of the liquid phase with MEF, which gives a total evaporation time of 50ms, with a heating time of 25ms. As MEF does not take into account the droplet number flux at size zero (as done for DQMOM in Fox et al. (2008)), the droplet number density is constant. Figure 4 shows the same quantites for MMEF, giving a total evaporation time of 400ms and a heating time of 150ms, respectively eight times and six times higher than from MEF. This is due to the presence of large droplets which heat and evaporate very slowly compared to smaller ones. As MMEF takes into account droplet number flux at size zero, the total droplet number decreases. Figure 4 also shows that the mean diameter does not become zero at the end of evaporation. This is due to the 1^{st} order of the multilfluid approach used here, which causes diffusion in phase space. This drawback was already shown in Laurent (2006), and can be tackle using higher order method with linear (Laurent (2006)) or exponential (Dufour et al. (2005)) reconstruction. This last one is a special case of a more general setting of Maximization of Entropy developped in Massot et al. (2010) and Kah et al. (2009). But this is not the scope of this work. This test case shows clearly that accounting for polydispersion is first order for the final application, as a monodisperse formalism highly underestimates heating and evaporation times.

Another interesting test case is related to drag, which also depend on droplet size and impacts the spatial dispersion. It is proposed here to analyse the spatial dispersion effects of a vortex having the same caracteristics than the swirl motion in MERCATO. The test case is then a two-dimensional frozen vortex, with a spatially homogeneous initial droplet distribution having the same velocity as the gas phase. Ten sections are used, with the same droplet number in each section. Radial velocity profile for the test case and in MERCATO at first position (13mm) are shown in Fig. 5. The computation is run for 5ms, which is the time needed by the liquid phase to impact the wall.

Figure 6 shows the number density and mean diameter radial profiles for both MEF and MMEF. After 5ms, droplet number density is widely distributed spatially in MMEF, while concentrated around 0.038m in MEF. Bigger droplets, due do the weaker influence of the gas phase, keep their initial velocity out of the vortex, and so

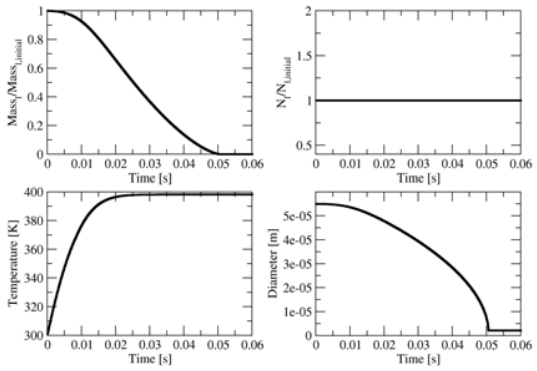

Figure 3: MEF Evaporation test case in MERCATO conditions. Evolution of total mass (upper left), droplet number density (upper right), liquid temperature (lower left) and mean diameter (lower right).

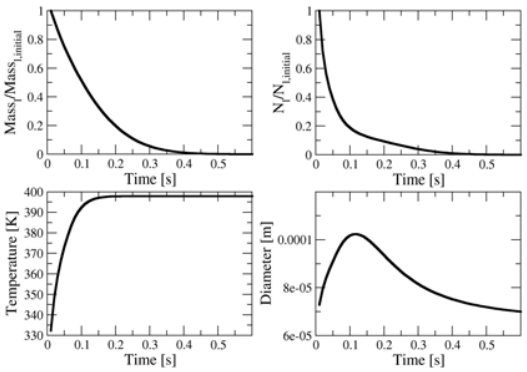

Figure 4: MMEF Evaporation test case in MERCATO conditions. Evolution of total mass (upper left), droplet number density (upper right), liquid temperature (lower left) and mean diameter (lower right).

their initial radial deviation. Small droplets are in equilibrium with the gas phase, so they reach a small velocity out of the vortex. The mean diameters are affected, with small diameters near the vortex center and big diameters far from. Two drawbacks are shown in Fig.6. The first drawback is linked to the mean diameter. In the center of the vortex, it is supposed to have no droplet, and so a mean diameter equal to zero. But the numerical scheme used here imposes to keep a low droplet number density, imposing a non-zero mean diameter. The second draw-

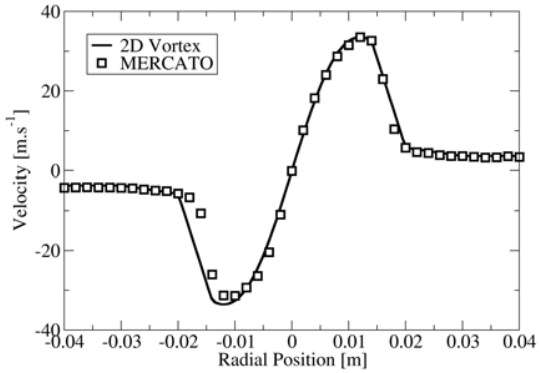

Figure 5: Gas velocity profile for the 2D vortex (solid line) and in MERCATO test case (13mm downstream the injection location)(squares).

back concerns the spatial dispersion. Considering drag force, each section behaves like its mean surface, and so follow only one trajectory. This is resulting in discrete accumulations for each class. In such a canonical test case, it seems to be relevant to tackle this issue. But in pratical cases, considering turbulent mixing and species diffusion , it has no effect on the fuel spatial dispersion.

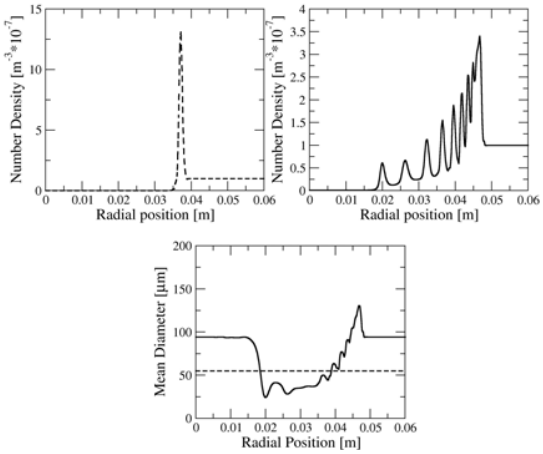

Figure 6: Radial distribution of droplet number density for MEF (top left) and MMEF (top right), and arithmetic mean diameter (bottom) for MEF (dashed line) and MMEF (solid line).

Simulation of the MERCATO test rig

Injecton is a keypoint in the simulation of two-phase flow burners. Then the injection system is modeled by the FIMUR model (Senoner et al. (2009a)), based on the model of Cossali (2000), and using autosimilarity assumptions for the velocity profiles. This model was initially designed for monodisperse injection, and the extension to multifluid injection is made by distributing the liquid volume fraction and droplet number density at all nodes over all diameters, following the size distribution of Fig. 2.

The computational domain is discretized with 1351767 tetrahedrons (Fig. 7). Averages are calculated during 40ms, which ensures statistical convergence.

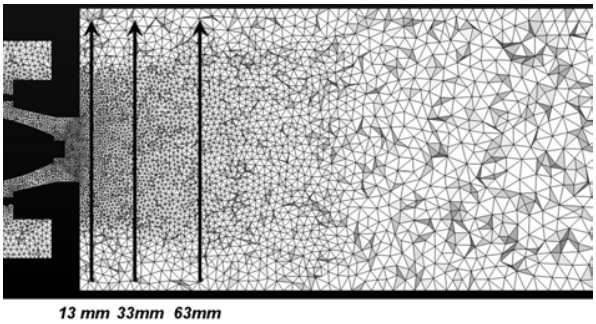

Figure 7: Mesh and velocity profiles position.

Figure 8 shows the total liquid volume fraction for MEF and MMEF computations. Firstly, due to its life time in a polydisperse framework (as shown in the evaporation test case), the liquid phase exists in the whole the combustion chamber for MMEF, whereas evaporates faster with the MEF. Secondly, due do the bigger inertia of large droplets, the liquid phase impacts the wall with MMEF, but not with the MEF.

Figure 9 shows the fuel mass fraction for MEF and MMEF computations, which is an important quantity for combustion. The two formalism lead to very different fuel repartitions. Due to the higher life time of droplet, the fuel mass fraction near the injection location is lower for the MMEF than for the MEF. More precisely, the high mass fraction zone around the injection location showed with MEF does not exist with the MMEF.

Velocity profiles at three downstream positions (13mm, 33mm and 63mm, Fig. 7) are compared to experimental data (Garcia-Rosa (2008)) for both MEF and MMEF results in Fig. 10-12. The axial velocity calculated with MEF and MMEF are in good agreement with experiments for the two first positions, and slightly underestimated inside the spray at the last position, although the outer zone is well captured by MMEF. Good

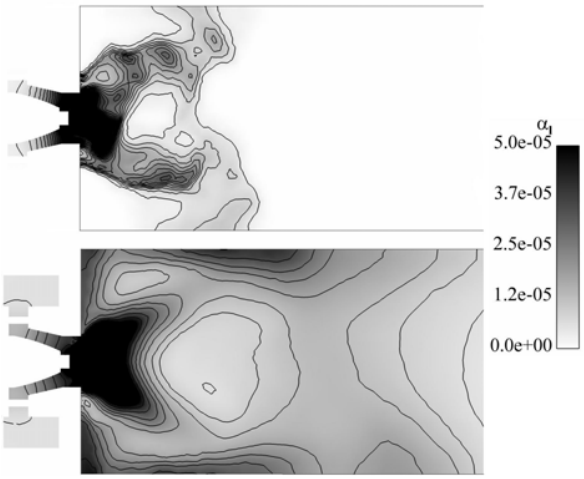

Figure 8: Instantaneous field of liquid volume fraction for MEF (up) and MMEF (down).

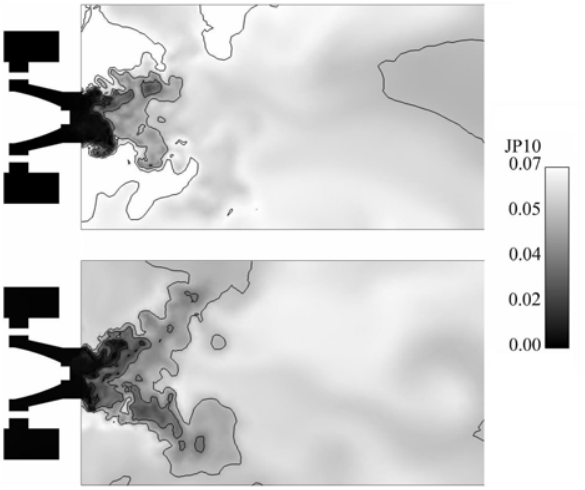

Figure 9: Instantaneous field of fuel mass fraction (JP10) for MEF (up) and MMEF (down).

agreement is also obtained for the radial velocity at the first position, but some discrepancies appear at the two other positions. MEF is not able to capture any behaviours, while MMEF reproduces the velocity in the outer zone. Finally, concerning the orthoradial velocity, it appears that MMEF reproduces the velocity profile accurately, while MEF catpures tendancies, but with less accurate results. Note that the good results for all velocity profiles at the first measurement location validate the injection methodology for both MEF and MMEF.

The Number Density Function (NDF) is compared to experimental data (Garcia-Rosa (2008)) at different points inside the burner (Fig. 13). Fig.14 shows that the NDF inside the spray (point 2) is well captured, whereas

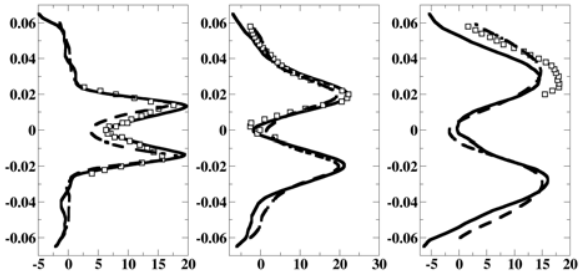

Figure 10: Axial velocity at 13mm (right), 33mm (center) and 63mm (left) for experiments (squares), MEF (full line) and MMEF (dashed line).

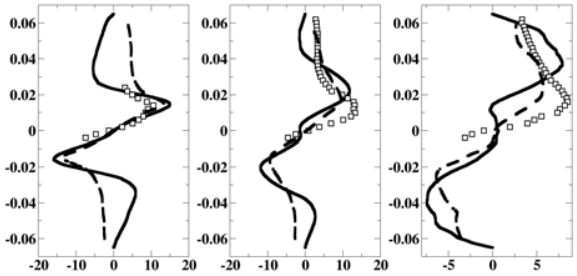

Figure 11: Radial velocity at 13mm (right), 33mm (center) and 63mm (left) for experiments (squares), MEF (full line) and MMEF (dashed line).

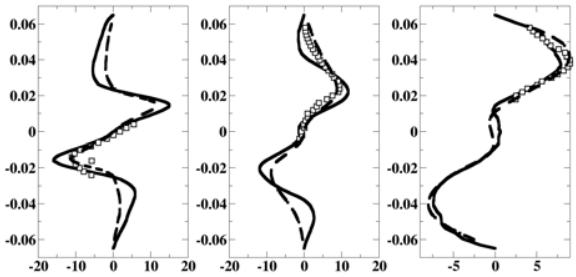

Figure 12: Orthoradial velocity at 13mm (right), 33mm (center) and 63mm (left) for experiments (squares), MEF (full line) and MMEF (dashed line).

the NDF in the center of the hollow cone (point 1) is shifted to big diameters. In Fig.15, the NDF in the center of the hollow cone (point 3) is not reproduced, but there the droplet number density is low both in measurements and computation. The NDF inside (point 4) and outside (point 5) the spray are well captured, with a good position of the maximum. In Fig.16, the NDF is well re-

produced at point 6 and point 8, especially considering the maximum. The NDF at point 7 is relatively well captured, but the position of the maximum is shifted to small diameters.

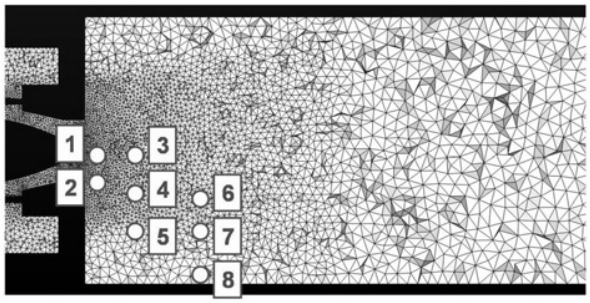

Figure 13: Mesh and NDF measurement location (circles)

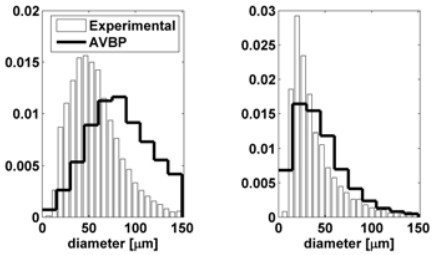

Figure 14: NDF at 13mm at point 1 (left) and point 2 (right) for MMEF (solid line) and experiment (histogram).

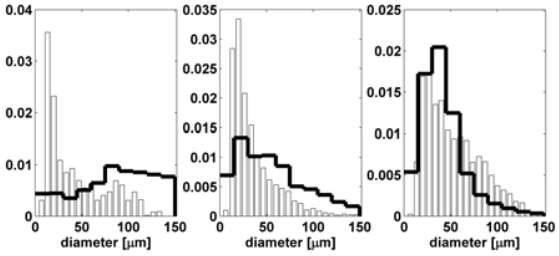

Figure 15: NDF at 33mm at point 3 (left), point 4 (center) and point 5 (right) for MMEF (solid line) and experiment (histogram).

Conclusions

Starting from the coupling of MEF and MA, the Multifluid Mesoscopic Eulerian Formalism (MMEF) has been

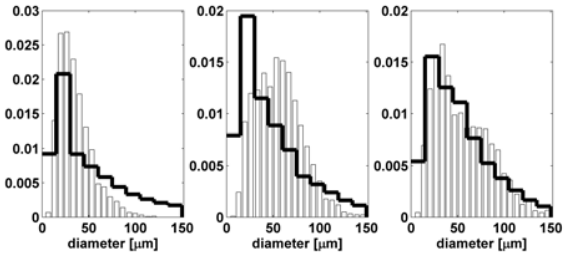

Figure 16: NDF at 63mm at point 6 (left), point 7 (center) and point 8 (right) for MMEF (solid line) and experiment (histogram).

derived. Preliminary test cases, designed to be representative of the final application, highlight the necessity to take into account polydispersion. However, they also show the limitation of numerical schemes used here to simulate a dispersed phase, especially in vaccum zones. Available numerical procedures allow to limitate the influence of this weakness.

Application of MMEF to the MERCATO test rig shows a good agreement between MMEF, MEF and experiments for velocity profiles at 9mm, making a good validation of the FIMUR injection strategy. For farther profiles (33mm and 63mm), MEF and MMEF show similar results in the central zone, but exhibit some discrepancies for the radial velocity. Only MMEF is able to capture the external zone, where mainly big droplets are present.

MMEF is also able to capture NDF profiles in the external zone (points 5 and 8). Results at other points show some discrepancies, although MMEF captures the global behaviour.

Such results confirm the necessity to take into account polydispersion in eulerian simulation of such aeronautical-type application. The main effect is the spatial segregation due to size/velocity correlations, which drive the drag force.

The next step of this work is to apply higher order multifluid approaches to the simulation of the MERCATO configuration. These methods use more than one moment for the liquid phase. As MEF is a two-moment method, the first step is to implement 2^{nd} order multifluid methods of Laurent (2006), Dufour et al. (2005). But the increase of order is coupled with the problem of the advection of moment sets, which needs to be adressed (Kah et al. (2009), Wright (2007)).

An other interesting and promising approach for such applications is the Direct Quadrature Method Of Moment Fox et al. (2008). In this approach, the pdf is not discretized into fixed sections, but is defined through a Gauss quadrature, and can be seen as a set of Diracs,

linked by a linear system. This approach has proven its ability to simulate evaporation and coalescence with very low diffusion in phase space, allowing to limit the number of Diracs compared to the number of sections needed by the classical multifluid approach. The original formalism has been extended by taking into account a velocity dispersion in Belt et al. (2009), and applied to the simulation of coalescence in Homogeneous Isotropic Turbulence in Wunsch et al. (2009).

Considering the evaporation, the strong influence of the droplet dissappearence with high order moment method or DQMOM is demonstrated in Fox et al. (2008). Modeled by a flux evaluated at zero size, a stable approach is shown in Fox et al. (2008), but its lack of precision needs further studies. A solution is proposed in Massot et al. (2010) with a high order moment method. In this approach, the pdf is defined by its four first moments. A reconstruction by Entropy Maximization allows to compute the evaporation flux at zero size. The pdf is then evaporated using an integrated formulation of the DQMOM approach. The robustness and the precision of this method has been proven in Massot et al. (2010), and make it a good candidate for final applications since it only involves one section, as long as the problem of moments set advection in complex industrial applications is addressed.

Acknowledgements

This research was supported by ANRT/IFP Ph.D. grant for A. Vié, DGA Ph.D. grant for M. Sanjosé.

References

Belt R.J. and Simonin O., Quadrature method of moments for the pdf modeling of droplet coalescence in turbulent two-phase flow, Proceedings of the ASME FEDSM 2009, FEDSM2009-78095, 2009

Boileau M., Simulations aux grandes échelles de l'allumage diphasique des foyers aéronautiques, Ph.D. thesis, Institut National Polytechnique de Toulouse, 2007

Colin 0. and Rudgyard M., Development of high-order Taylor-Galerkin schemes for unsteady calculations, Journal of Computational Physics, Vol. 162(2), pp. 338-371, 2000

Cossali G.E., An integral model for gas entrainment into full cone sprays, Journal of Fluid Mechanics, Vol. 439(2), pp. 353-366, 2001

De Chaisemartin S., Modèles eulériens et simulation de la dispersion turbulente de brouillards qui s'évaporent, Ph.D. thesis, Ecole Centrale Paris, 2009, available on TEL http://tel.archives-ouvertes.fr/tel-00443982/en

Dufour G. and Villedieu P., A second-order multi-fluid model for evaporationg sprays, Mathematical Modelling and Numerical Analysis, Vol. 39(5), pp. 931-963, 2005

Février P., Simonin O. and Squires K.D., Partitioning of particle velocities in gas-solid turbulent flow into a continuous field and a spatially uncorrelated random distribution: theoretical formalism and numerical study, Journal of Fluid Mechanics, Vol. 533, pp. 1-46, 2005

Fox R.O., Laurent F. and Massot M., Numerical simulation of spray coalescence in an Eulerian framework: Direct quadrature method of moments and multi-fluid method, Journal of Computational Physics, Vol. 227, pp. 3058-3088, 2008

Garcia M., Development and validation of the Euler-Lagrange formulation on a parallel and unstructured solver for large-eddy simulation, Ph.D. thesis, Université de Toulouse, Toulouse, 2009, available on TEL http://tel.archives-ouvertes.fr/tel-00414067/en/

Garcia-Rosa N., Phénomènes d'allumage d'un foyer de turbomachine en conditions de haute altitude, Ph.D. thesis, Université de Toulouse, Toulouse, 2008

Greenberg J.B., Silverman I. and Tambour Y., On the origin of spray sectional conservation equations, Combustion and Flame, Vol. 93, pp. 90-96, 1993

Kah D., Laurent F., Massot M. and Jay S., Modeling of polydisperse sprays using a high order method for numerical advection of size moments, 11th International Conference of Liquid Atomization and Spray Systems, Vail, USA, July 2009

Kaufmann A., Moreau M., Simonin O. and Helie J., Comparison between Lagrangian and mesoscopic Eulerian modelling approaches for inertial particles suspended in decaying isotropic turbulence, Journal of Computational Physics, Vol. 227(13), pp. 6448-6472, 2008

Kuo K., Principles of Combustion, Wiley-Interscience, New York, 2nd edition, 2005

Laurent F. and Massot M., Multi-fluid modeling of laminar poly-dispersed spray flames: origin, assumptions and comparison of sectional and sampling methods, Comustion Theory and Modelling, Vol. 5, pp. 537-572, 2001

Laurent F., Massot M. and Villedieu P., Eulerian multi-fluid modeling for the numerical simulation of coalescence in polydisperse dense liquid sprays,Journal of Computational Physics, Vol. 194, pp. 505-543, 2004

Laurent F., Numerical analysis of eulerian multi-fluid models in the context of kinetic formulations for dilute evaporating sprays, Mathematical Modeling and Numerical Analysis, Vol. 3, pp. 431-468, 2006

Masi E., Riber E., Sierra P., Simonin O. and Gicquel L.Y.M., Modeling the random uncorrelated velocity stress tensor for unsteady particle eulerian simulation in turbulent flows, International Conference on Multiphase Flow, Tampa, US, 2010

Massot M., Knikker R., Péra C. and Réveillon J., Lagrangian/Eulerian analysis of the dispersion of evaporating droplets in a non-homogeneous turbulent flow, International Conference on Multiphase Flow, Yokohama, Japan, 2004

Massot M., Eulerian Multi-Fluid Models for Polydisperse Evaporating Sprays, CISM - International Centre for Mechanical Sciences - Courses and Lecture Series, Vol. 492, 2007

Massot M., Laurent F., Kah D. and de Chaisemartin S., A robust moment method for evaluation of the disappearance rate of evaporating sprays, SIAM Journal of Applied Mathematics, 2010, available on HAL http://hal.archives-ouvertes.fr/hal-00332423/en/

Moreau M., Bédat B. and Simonin O., Development of gas-particle euler-euler LES approach: a priori analysis of particle sub-grid models in homogeneous isotropic turbulence, Flow Turbulence and Combustion, Vol. 84(2), pp.295-324, 2010

Nicoud F. and Ducros F., Subgrid-scale stress modelling based on the square of the velocity gradient, Flow Turbulence and Combustion, Vol. 62(3), pp.183-200, 1999

Réveillon J., Massot M. and Péra C., Analysis and modelling of the dispersion of vaporizing polydispersed sprays in turbulent flows, Center of Turbulence Research, Proceedings of The Summer Program, 2002

Sanjosé M., Lederlin T., Gicquel L., Cuenot B., Pitsch H., Garcia-Rosa N., Lecourt R. and Poinsot T., LES of two-phase reacting flows, Center of Turbulence Research, Proceedings of The Summer Program, 2008

Sanjosé M., Évaluation de la méthode Euler-Euler pour la simulation numérique aux grandes échelles des chambres à carburant liquide , Ph.D. thesis, Université de Toulouse, Toulouse, 2009

Sazhin S.S., Advanced models of fuel droplet heating and evaporation, Progress in Energy and COmbustion Sciences, Vol. 32, pp.162-214, 2006

Senoner J.M., Sanjosé M., Cuenot B. and Poinsot T., A methodology to model fuel injection by pressure-swirl atomizer for large eddy simulation of real combustion chamber, to be submitted to American Institute of Aeronautics and Astronautics Journal, 2009a

Senoner J.M., Sanjosé M., Lederlin T., Jaegle F., Garcia M., Riber E., Cuenot B., Gicquel L., Pitsch H. and Poinsot T., Eulerian and lagrangian large eddy simulations of an evaporating two-phase flow, Compte rendu de l'Academie des Sciences, Vol. 337(6-7),pp. 458-468, 2009b

Sirignano W.A., Fluid dynamics and transport of droplets and sprays, Cambridge University Press, New York, USA, 1999

Vié A., Martinez L., Jay S., Benkenida, A. and Cuenot B., Validation of the eulerian mesoscopic approach in particle-charged homogeneous isotropic decaying turbulence in the scope of large eddy simulation of fuel sprays, 11th International Conference of Liquid Atomization and Spray Systems, Vail, USA, July 2009

Williams F.A., Spray Combustion and atomization, Physics of Fluids, Vol. 1, pp.541-545, 1958

Wright D.L., Numerical advection of moments of the particule size distribution in Eulerian models, Journal of Aerosol Science, pp. 352-369, 2007

Wunsch D., Belt R.J., Fede P. and Simonin O., DNS/DPS of inertial droplet coalescence in Homogeneous Isotropic Turbulence and comparison with pdf model predictions using the direct quadrature method of moments, Proceedings of the ASME FEDSM 2009, FEDSM2009-78091, 2009